

# The effects of undercooling and deformation rates on the crystallization kinetics of Stromboli and Etna basalts

A. Vona · C. Romano

Received: 10 October 2012 / Accepted: 13 May 2013 / Published online: 28 May 2013  
© Springer-Verlag Berlin Heidelberg 2013

**Abstract** We have investigated the effect of undercooling and deformation on the evolution of the texture and the crystallization kinetics of remelted basaltic material from Stromboli (pumice from the March 15, 2007 paroxysmal eruption) and Etna (1992 lava flow). Isothermal crystallization experiments were conducted at different degrees of undercooling and different applied strain rate ( $T = 1,157\text{--}1,187\text{ °C}$  and  $\dot{\gamma}_i = 4.26\text{ s}^{-1}$  for Stromboli;  $T = 1,131\text{--}1,182\text{ °C}$  and  $\dot{\gamma}_i = 0.53\text{ s}^{-1}$  for Etna). Melt viscosity increased due to the decrease in temperature and the increase in crystal content. The mineralogical assemblage comprises  $Sp + Plg$  (dominant)  $\pm Cpx$  with an overall crystal fraction ( $\phi$ ) between 0.06 and 0.27, increasing with undercooling and flow conditions. Both degree of undercooling and deformation rate deeply affect the kinetics of the crystallization process. Plagioclase nucleation incubation time strongly decreases with increasing  $\Delta T$  and flow, while slow diffusion-limited growth characterizes low  $\Delta T$ —low deformation rate experiments. Both Stromboli (high strain rate) and Etna (low strain rate) plagioclase growth rates ( $G$ ) display relative small variations with Stromboli showing higher values ( $4.8 \pm 1.9 \times 10^{-9}\text{ m s}^{-1}$ ) compared to Etna ( $2.1 \pm 1.6 \times 10^{-9}\text{ m s}^{-1}$ ). Plagioclase average nucleation rates  $J$  continuously increase with undercooling from  $1.4 \times 10^6$  to  $6.7 \times 10^6\text{ m}^{-3}\text{ s}^{-1}$  for Stromboli and from  $3.6 \times 10^4$  to  $4.0 \times 10^6\text{ m}^{-3}\text{ s}^{-1}$  for Etna. The extremely low value of  $3.6 \times 10^4\text{ m}^{-3}\text{ s}^{-1}$  recorded at the lowest undercooling experiment for Etna

( $\Delta T = 20\text{ °C}$ ) indicates that the crystallization process is growth-dominated and that possible effects of textural coarsening occur.  $G$  values obtained in this paper are generally one or two orders of magnitude higher compared to those obtained in the literature for equivalent undercooling conditions. Stirring of the melt, simulating magma flow or convective conditions, facilitates nucleation and growth of crystals via mechanical transportation of matter, resulting in the higher  $J$  and  $G$  observed. Any modeling pertaining to magma dynamics in the conduit (e.g., ascent rate) and lava flow emplacement (e.g., flow rate, pāhoehoe—‘a‘ā transition) should therefore take the effects of dynamic crystallization into account.

**Keywords** Basalts · Plagioclase · CSD · Nucleation · Growth · Crystallization kinetics

## Introduction

The number, size and shape of crystals in a rock reflect the relative kinetics of nucleation and growth, which are in turn dependent on the magma solidification history. Controlling the cooling history by experimental studies, a quantitative relationship between the solidification process and crystallization kinetics can be determined. The observed textures of experimental samples can be used to constrain nucleation and growth rates during crystallization. Applying the experimentally derived kinetic parameters to natural magmatic rocks can in turn give us information about their solidification history. Textural variations in igneous rocks have frequently been quantified in terms of changes in the crystal size distribution (CSD: Cashman and Marsh 1988; Marsh 1988) as CSD curves can be linked to kinetic processes (Marsh 1998, 2007; Armienti 2008).

---

Communicated by J. Blundy.

---

A. Vona (✉) · C. Romano  
Dipartimento di Scienze, Università degli Studi Roma Tre,  
L.go San Leonardo Murialdo 1, 00146 Rome, Italy  
e-mail: alessandro.vona@uniroma3.it

Most experimental studies have focused their attention on the effects of temperature (i.e., initial melting temperature, cooling rate or degree of undercooling) on rock textures, nucleation and growth rates and crystal morphology (e.g., Lofgren 1974, 1980, 1983; Sato 1995; Burkhard 2002; Zieg and Lofgren 2006; Iezzi et al. 2008; Orlando et al. 2008; Pupier et al. 2008). Even though most studies recognize the importance of flow (or convection) in defining the crystallization kinetics in magmas (Emerson 1926; MacDonalds 1953; Kouchi et al. 1986; Sato 1995; Cashman et al. 1999), only Kouchi et al. (1986) examined this effect experimentally.

Isothermal crystallization experiments on Stromboli and Etna basalts were conducted by Vona et al. (2011) to investigate the rheological behavior of magmatic suspensions. The authors performed a detailed textural characterization of the samples (crystal fraction, crystal shape, size and orientation distributions) to constrain a model for the effect of crystals on the rheology of magmatic suspensions. As the crystallization experiments were performed at controlled chemical and physical conditions, in this contribution, we explore the effects of undercooling and stirring on the evolution of the texture and the crystallization kinetics of basalts.

### Starting materials and experimental setup

The present study has been carried out on remelted materials from Stromboli and Etna. The Stromboli sample was a pumice emitted during March 15, 2007 paroxysmal eruption. The pumice is nearly aphyric (phenocryst content  $\phi < 0.05$ ), with microphenocrysts of clinopyroxene and olivine in a HK-basaltic glassy matrix, and is representative of the volatile-rich, low porphyritic magma (LP; Landi et al. 2009) erupted during paroxysms at Stromboli (Table 1). The Etna sample was collected from the 1991 to 1993 eruption lava flow field in Val Calanna, ca. 6.5 km from the eruptive fissure (Calvari et al. 1994). The 1991–1993 Etna eruption represents one of the most prolonged and volumetrically significant eruptions observed at Etna over the last three centuries (Armienti et al. 1994; Calvari et al. 1994), and its trachybasaltic composition is representative of the more recent eruptive history at Etna (Orlando et al. 2008; Table 1). The rock has a porphyritic texture ( $\phi \sim 0.3$ ) with phenocrysts represented by plagioclase ( $\phi \sim 0.17$ ), olivine ( $\phi \sim 0.08$ ), augitic clinopyroxene ( $\phi \sim 0.03$ ) and titanomagnetite ( $\phi \sim 0.01$ ).

The technique used to perform the isothermal crystallization experiments has been described in detail by Vona et al. (2011). The experiments were carried out in air and at 1 atm pressure in a box furnace heated by MoSi<sub>2</sub> elements, under stirring conditions by using a Brookfield DV-III+ viscometer head. The stirring spindle used for this study was 3.2 mm in

**Table 1** Chemical composition of starting material

	Stromboli HK-basalt	Etna Trachybasalt
SiO <sub>2</sub>	50.35 (0.16)	48.16 (0.23)
TiO <sub>2</sub>	0.92 (0.05)	1.69 (0.06)
Al <sub>2</sub> O <sub>3</sub>	17.18 (0.10)	17.10 (0.11)
FeO	1.71 (0.11)	2.49 (0.10)
Fe <sub>2</sub> O <sub>3</sub>	7.04 (0.12)	8.60 (0.10)
MnO	0.18 (0.04)	0.19 (0.02)
MgO	6.28 (0.06)	5.38 (0.08)
CaO	11.64 (0.16)	10.36 (0.07)
Na <sub>2</sub> O	2.33 (0.04)	3.69 (0.05)
K <sub>2</sub> O	1.85 (0.05)	1.91 (0.03)
P <sub>2</sub> O <sub>5</sub>	0.53 (0.07)	0.43 (0.06)
Total	99.17	99.41

Oxide compositions are normalized to a total of 100 wt%

Numbers in brackets correspond to 1 $\sigma$  standard deviation

Measured totals are also reported

diameter, 42 mm in length with a 45° conical tip to reduce end effects. Crystallization experiments were performed at different degrees of undercooling in the temperature range  $T = 1,157$ – $1,187$  °C for Stromboli and  $T = 1,131$ – $1,182$  °C for Etna (Fig. 1). Prior to lowering the temperature at *subliquidus* conditions, both magmas experienced the same *superliquidus* treatment. They were stirred continuously at  $T = 1,400$  °C for 5 h to ensure that all of the natural crystalline phases present in the starting materials were fully dissolved. Subsequently, the temperature of the melt was lowered rapidly to that of the dwell temperature. Melt viscosity, which increased due to decreasing temperature and increasing crystal content, was continuously monitored. The viscosity reading typically achieved a steady value after  $10^4$ – $10^5$  s (interpreted here as equilibrium in the crystallization process at each temperature).

The main difference between the two data sets on Stromboli and Etna is given by the initial strain rate adopted during the experiments. Different initial deformation rates were applied by setting different stirring velocities. The initial rotational speed was set to  $\omega = 20$  rpm for experiments carried out on Stromboli material and to  $\omega = 2.5$  rpm for Etna samples. These speeds translate into a maximum initial strain rate of  $\dot{\gamma}_i = 4.26$  s<sup>-1</sup> and  $\dot{\gamma}_i = 0.53$  s<sup>-1</sup> for Stromboli and Etna samples, respectively. During the experiments, the software controlling the spindle speed automatically halves the speed when maximum torque (and hence maximum viscosity for that speed) is reached. As crystallization induces an increase in magma viscosity, most experiments are performed in a deformation regime in which the strain rate decreases with time. Details on the deformation rate versus time path are reported in Fig. 2.

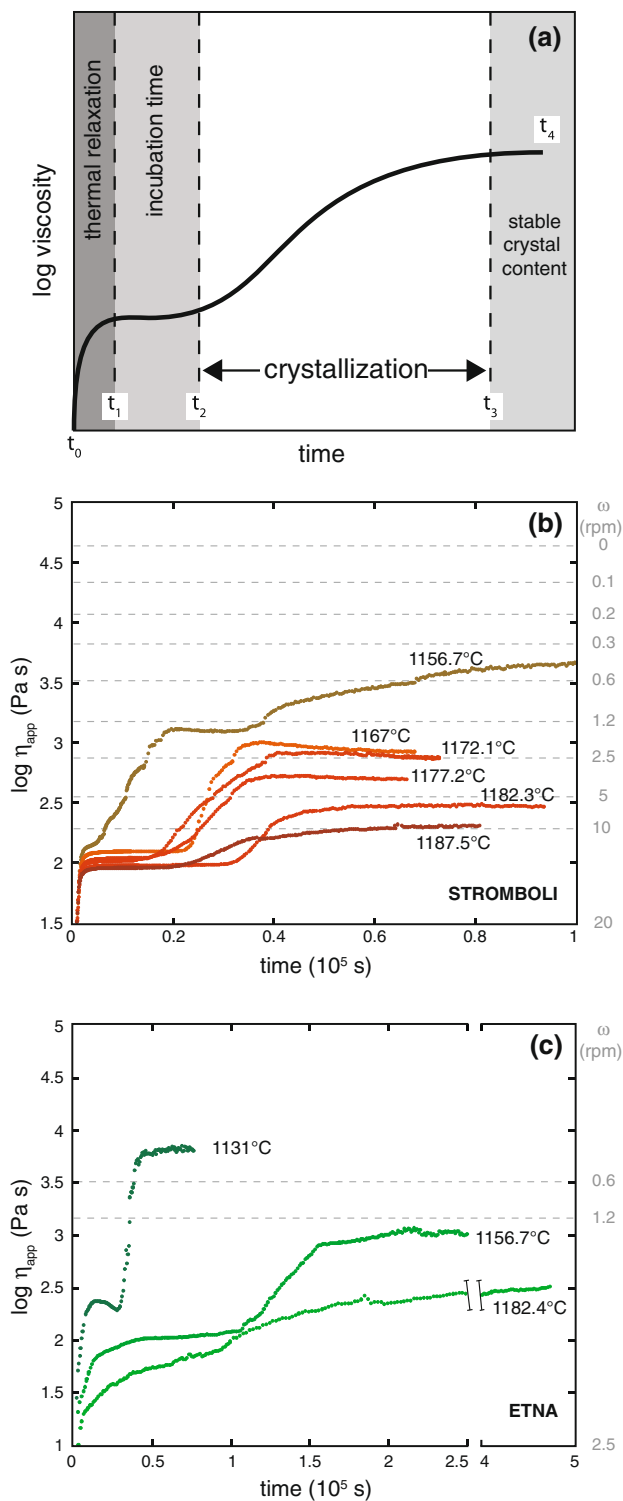


**Fig. 1** Viscosity-time path of crystallization experiments. **a** Identification of kinetic processes. As a general trend, four regions can be recognized with increasing experimental time ( $t$ ): (1)  $t_0$ – $t_1$ : viscosity increase due to thermal relaxation of the melt at the dwell temperature; (2)  $t_1$ – $t_2$ : time-invariant viscosity of the metastable liquid before crystallization. The length of this plateau reflects the incubation time; (3)  $t_2$ – $t_3$ : viscosity increase due to crystallization; (3)  $t_3$ – $t_4$ : time-invariant viscosity of the crystal-bearing magma with a stable crystal content. Time  $t_4$  indicates the time at which the rheological measurements were interrupted. **b–c** Temporal evolution of viscosity for Stromboli (**b**) and Etna (**c**) during isothermal crystallization experiments (redrawn from Vona et al. 2011). Viscosity increase due to crystallization causes a decrease in rotational speed  $\omega$  (indicated on the right y-axis)

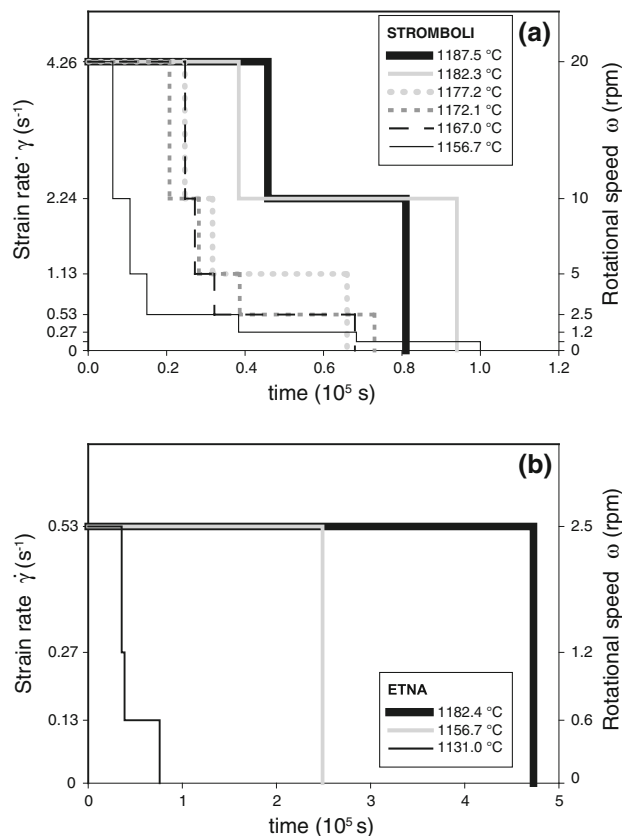


**Fig. 2** Deformation rate [expressed as strain rate ( $s^{-1}$ ) and rotational speed (rpm)] versus time ( $10^5$  s) for **a** Stromboli and **b** Etna. The strain rate decreases with time for all the experiments, with the exceptions of two Etna measurements ( $T = 1,156.7$  °C and  $T = 1,182.4$  °C) performed at a constant strain rate of  $0.53$   $s^{-1}$

At the end of each experiment, the samples were removed from the furnace and allowed to cool in air inside the crucible. The post-run products were then drilled from the crucible, and the cylindrical cores (20 mm diameter  $\times$  40 mm length) were sectioned at surfaces parallel and perpendicular to the rotational axis, for subsequent

chemical and textural analyses. To avoid thermal cracking during cooling which could have prevented the collection of intact cores by drilling, samples were not rapidly quenched. During air quenching, however, small quench crystals forming in the minutes timescale during cooling from experimental dwell temperature ( $T_{exp}$ ) to the glass transition temperature ( $T_g$ ) are expected. Quench rate ( $q_{air}$ ) of our experiments was calibrated inserting a thermocouple inside the liquid once extracted from the rheometer. In

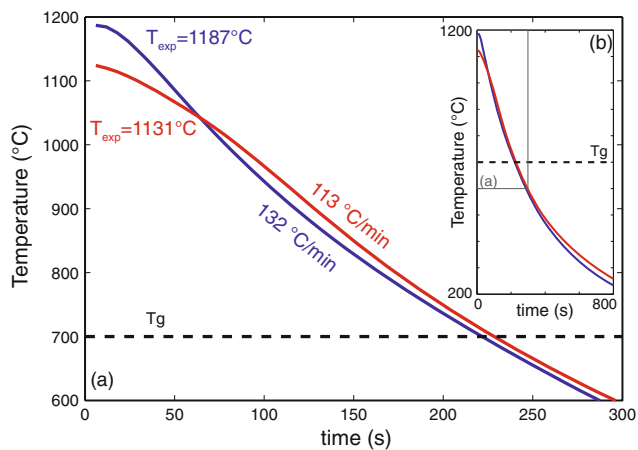


**Fig. 3** Calibration experiments performed to measure quench rates for two limiting temperatures of  $T_{\text{exp}} = 1,187^\circ\text{C}$  (blue) and  $T_{\text{exp}} = 1,131^\circ\text{C}$  (red). **a** Detail of the first 300 s of the experiments, whose entire duration are reported in the inset **(b)**. Linear approximations of the first 300 s (down to  $T = 600^\circ\text{C}$ ) indicate cooling rates of  $132^\circ\text{C}/\text{min}$  and  $113^\circ\text{C}/\text{min}$  corresponding to quenching temperatures of  $T_{\text{exp}} = 1,187^\circ\text{C}$  and  $T_{\text{exp}} = 1,131^\circ\text{C}$ , respectively. Black dashed line displays glass transition temperature ( $T_g$ ) corrected for cooling rate after Giordano et al. (2008a). Time to reach  $T_g$  from dwell temperatures, corresponding to time allowed for quench crystallization varies from 220 s (3.6 min) to 228 s (3.8 min)

Fig. 3, the results of the calibration runs for two limiting temperatures of 1,187 and 1,131 °C are displayed. As it can be seen, temperature decreases in a linear fashion down to about 600 °C for both experiments. For  $T > 600^\circ\text{C}$ , we calculate a gradient of  $q_{1,131} = 113$  and  $q_{1,187} = 132^\circ\text{C}/\text{min}$  for low- and high-temperature experiments, respectively. To measure the glass transition temperature (that defines the transition from a liquid-like to a solid-like response of a magma), we first consider  $T_g$  measured via calorimetry at  $q = 5, 10$  and  $20^\circ\text{C}/\text{min}$  (e.g., for Etna basalt  $666^\circ\text{C}$  at  $q = 5^\circ\text{C}/\text{min}$ ;  $673^\circ\text{C}$  at  $q = 10^\circ\text{C}/\text{min}$ ; and  $681^\circ\text{C}$  at  $q = 20^\circ\text{C}/\text{min}$ ; Di Genova, pers. comm.). Given their similar chemical compositions, Etna and Stromboli basalts display very similar  $T_g$ . Starting from these  $T_g$  values, we have extrapolated  $T_g$  at our cooling rates, considering a linear correlation between  $T_g$  and  $\log_{10} q$  (Giordano et al. 2008a). Values of  $T_g = 700 \pm 3^\circ\text{C}$  were obtained for both compositions and all the examined quenching rates. Time to reach  $T_g$  from dwell temperatures varies from 220 s (3.6 min) to 228 s (3.8 min) for all the dataset of the present study.

## Experimental results

The chemical and textural analyses performed to characterize the post-run products of isothermal crystallization experiments on basaltic magmas from Stromboli and Etna were described in Vona et al. (2011). They indicated that

the high-temperature mineralogical assemblage is dominated by the presence of spinel (minor) and plagioclase with the occurrence of stable clinopyroxene only at the lowest temperatures ( $1,157$  and  $1,131^\circ\text{C}$  for the Stromboli and the Etna samples, respectively; Fig. 4). Plagioclase compositions are within the range of natural magmas from Stromboli and Etna and are comprised between  $\text{An}_{79-72}$  and  $\text{An}_{72-64}$  for Stromboli and Etna, respectively, with the anorthite content decreasing with decreasing temperature. Plagioclase crystals frequently show a skeletal habit and are elongate in shape (Fig. 4). Clinopyroxene is augitic in composition, only slightly elongate with average aspect ratios of 2.

The overall crystal fractions ( $\phi$ ) obtained by image analyses are in agreement with mass balance calculations and vary between 0.06 and 0.27, with plagioclase crystal contents between  $\phi = 0.11-0.23$  for Stromboli and between  $\phi = 0.06-0.18$  for Etna. MELTS simulations (Ghiorso and Sack 1995; Asimow and Ghiorso 1998) indicate the same crystallization sequence where the spinel is the *liquidus* phase, and the onset of plagioclase and clinopyroxene crystallization occurs at  $T_{\text{m(plg)}} = 1,212.5^\circ\text{C}$  and  $T_{\text{m(cpx)}} = 1,194^\circ\text{C}$  for Stromboli and at  $T_{\text{m(plg)}} = 1,203^\circ\text{C}$  and  $T_{\text{m(cpx)}} = 1,182^\circ\text{C}$  for Etna, respectively. For both Stromboli and Etna, the MELTS crystallization temperatures for clinopyroxenes are always higher compared to the experimental values. As for the spinel, the percentage of spinel crystals is overestimated by the calculator, but the predicted increase in spinel mass with decreasing  $T$  is very similar to that found in experiments. The predicted plagioclase mass proportions fit quite well the values obtained by textural analyses for Stromboli. For Etna, a discrepancy between measured and calculated values ( $\sim 8\%$ ) was found at the lowest temperature. On the basis of the calculated crystallization onsets ( $T_{\text{m}}$ ), we derive that the experiments were run at nominal degree of undercooling ( $\Delta T_0 = T_{\text{m}} - T_{\text{exp}}$ ) varying from  $24.5$  to  $55.8^\circ\text{C}$  for Stromboli and from  $20.6$  to  $72^\circ\text{C}$  for Etna with respect to the plagioclase phase. During the experiments, the change in residual melt chemical composition due to crystallization yields changes in the melt *liquidus* temperature; hence, the reported degrees of undercooling represent nominal  $\Delta T$  (e.g., Orlando et al. 2008).

The temporal variations in viscosity have been used to constrain the time for the crystallization process. In fact, all rheological measurements were stopped after the achievement of a time-invariant value of viscosity ( $t_3-t_4$  plateau in Fig. 1a), which was interpreted as indicative of the attainment of a stable crystal content. Therefore, the time to reach the plateau is considered as the time in which the crystallization process takes place ( $t_3$  in Fig. 1a; Table 2). The uncertainty in the location of this time-viscosity value has been evaluated to be approximately 10 %. Two exceptions

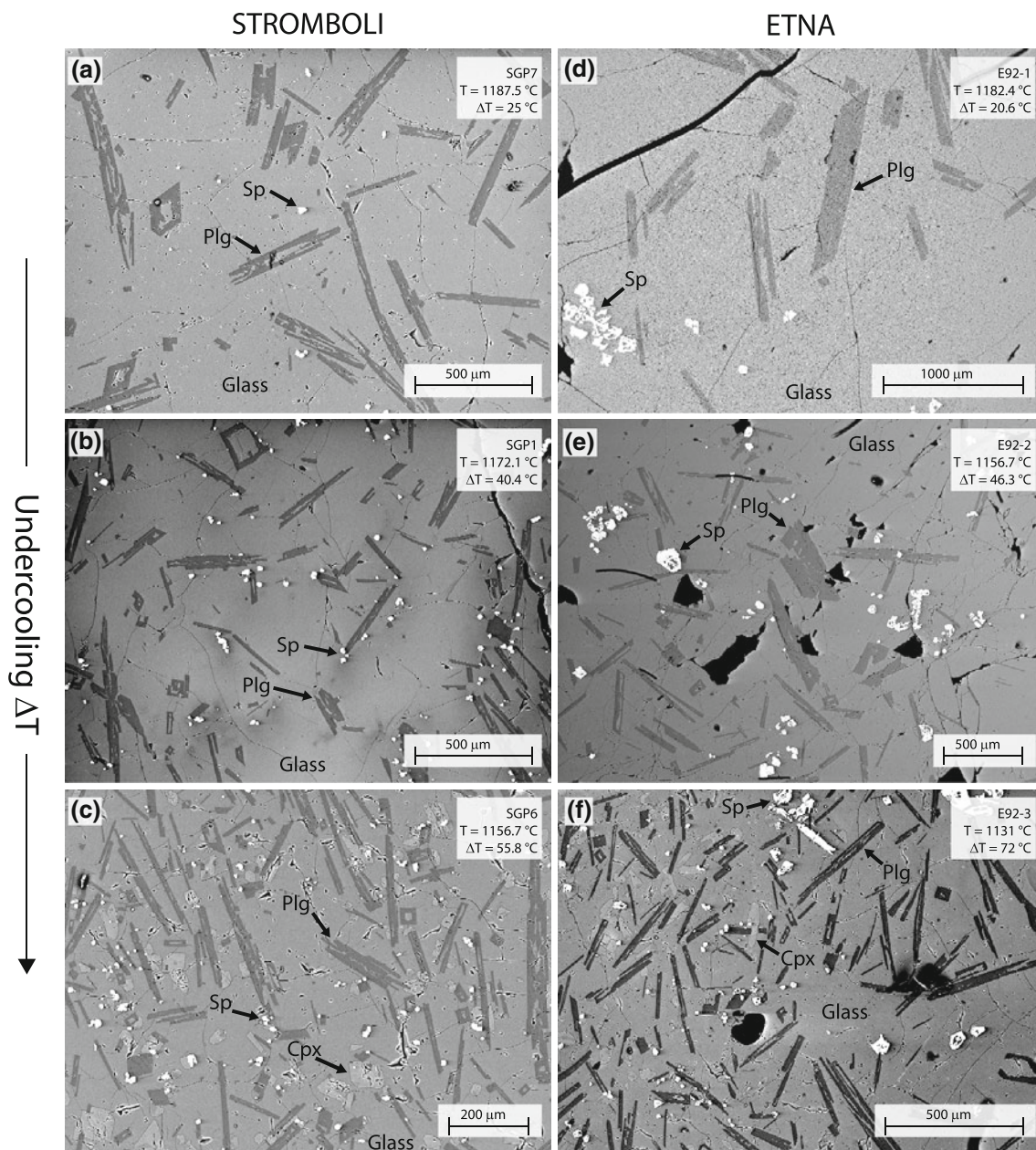


**Fig. 4** Photomicrographs of thin sections of the experimental products from Stromboli (a–c) and Etna (d–f) performed at different undercoolings. *Sp* Spinel; *Plg* plagioclase; *Cpx* Clinopyroxene

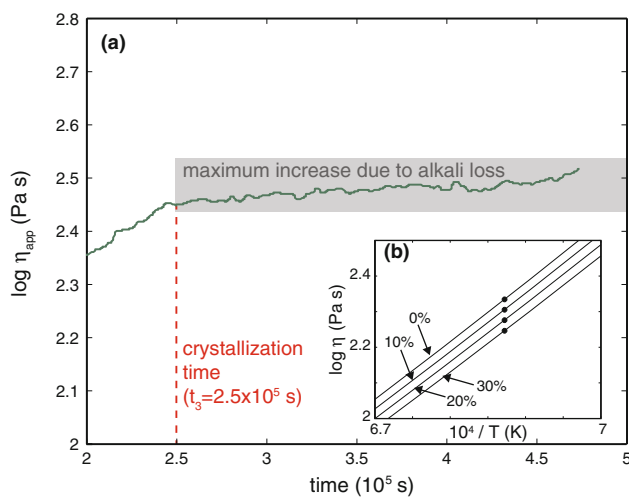
are given by the lowest-temperature experiment on Stromboli (SGP6;  $T = 1,156.7\text{ }^{\circ}\text{C}$ ) and by the highest-temperature experiment on Etna (E92-1;  $T = 1,182.4\text{ }^{\circ}\text{C}$ ), showing more complex temporal variations in viscosity. In the first case (SGP6), viscosity increased in a stepwise fashion with the formation of an intermediate viscosity plateau (Fig. 1b). The cause of this plateau is difficult to ascertain. One possible explanation could be the progressive saturation of plagioclase and the subsequent onset of clinopyroxene crystallization. In this case, a value of  $t_3 = 2\text{--}4 \times 10^4\text{ s}$  should be chosen. However, a secondary plateau was not observed for the lowest-temperature Etna sample (E92-3;  $T = 1,131\text{ }^{\circ}\text{C}$ ;

Fig. 1c) in which clinopyroxene is also present. Given the uncertainty on the interpretation of the viscosity-time curve, for this experiment only, we calculated the experimental crystallization time for plagioclases as the time interval between the occurrence of the first and the second plateaus (i.e., for  $t_3 = 2\text{--}7 \times 10^4\text{ s}$ ).

The highest-temperature experiment on Etna sample (E92-1;  $T = 1,182.4\text{ }^{\circ}\text{C}$ ) shows the longest duration among the entire experimental dataset. For this experiment, a slow continuous viscosity rise has been observed, and a real time-invariant value of viscosity was not achieved for time up to  $t_4 = 47 \times 10^4\text{ s}$  (Figs. 1c, 5). However, the slow continuous

**Table 2** Experimental temperature and time conditions

Run	Stromboli						Etna		
	SGP7	SGP5	SGP4	SGP1	SGP3	SGP6	E92-1	E92-2	E92-3
$T_{\text{exp}}$ (°C)	1,187.5	1,182.3	1,177.2	1,172.1	1,167	1,156.7	1,182.4	1,156.7	1,131
$\Delta T_0$ (pIlg) (°C)	25	30.2	35.3	40.4	45.5	55.8	20.6	46.3	72
Initial strain rate (s <sup>-1</sup> )	4.26	4.26	4.26	4.26	4.26	4.26	0.53	0.53	0.53
Time (10 <sup>4</sup> s)									
$t_1$	0.3	0.3	0.3	0.3	0.3	0.2	3.1	1.2	0.7
$t_2$	2.2	3.1	1.4	1.5	2.7	0.4	9.5	10.5	2.8
$t_3$	5.0	4.8	3.7	4.2	3.7	(2–7)	25.0	16.1	4.2
$t_4$	8.1	9.4	6.6	7.3	6.8	10	47.3	24.9	7.6
Time at $\Delta T = \Delta T_0$ (10 <sup>4</sup> s)									
$t_{3/2}$	2.5	1.6	0.7	2.1	1.9	(1–3.5)	12.5	8.1	2.1



**Fig. 5** Evaluation of possible sodium loss for the highest-temperature experiment on Etna sample (E92-1;  $T = 1,182.4$  °C). **a** Viscosity-time record of the final section of the experiment showing a slow viscosity rise up to  $t_4 = 4.7 \times 10^5$  s. **b** Effect of alkali loss on the viscosity of the residual liquid calculated after Giordano et al. (2008b) model, assuming different  $\text{Na}_2\text{O}$  wt% content ( $\text{Na}_2\text{O} = 4.07, 4.48, 4.88, \text{ and } 5.29$  wt%), representing 0, 10, 20 and 30 % of sodium loss. Maximum viscosity variation is lower than 0.1  $\log_{10}$  units and resembles the viscosity rise experienced by E92-1, which could be related to a small amount of alkali loss. The final equilibration time for this experiment has been then taken at  $t_3 = 2.5 \times 10^5$  s

viscosity rise could be related not to a crystallization increase, but to a slow change in chemistry of the residual liquid. In particular, it is possible that the liquid experienced a certain degree of sodium evaporation with time. To correct for this, and to constrain the crystallization timeframe, we tried to evaluate the effect of alkali loss on the viscosity of the residual liquid. Using Giordano et al. (2008b) model, we calculated on chemical basis the viscosity of E92-1 residual liquid (in wt%  $\text{SiO}_2 = 51.09$ ;  $\text{TiO}_2 = 1.82$ ;  $\text{Al}_2\text{O}_3 = 16.34$ ;  $\text{FeO}_{\text{tot}} = 8.01$ ;  $\text{MnO} = 0.22$ ;  $\text{MgO} = 5.43$ ;  $\text{CaO} = 10.36$ ;  $\text{Na}_2\text{O} = 4.07$ ;  $\text{K}_2\text{O} = 2.05$ ;  $\text{P}_2\text{O}_5 = 0.61$ ; from Vona et al. 2011), assuming different  $\text{Na}_2\text{O}$  content, ( $\text{Na}_2\text{O} = 4.07,$

4.48, 4.88, and 5.29 wt%), simulating in this way 0, 10, 20 and 30 % of sodium loss, respectively. As it can be seen from Fig. 5b, at  $T = 1,182$  °C, a 30 % of alkali loss yields a viscosity variation of  $\Delta \log_{10} \eta$  up to 0.1 Pa s, which resembles the variation of  $\eta$  experienced by sample E92-1. The very small but systematic drift of viscosity with time observed for sample E92-1 could be potentially related to a certain alkali loss experienced for this experiment. For this reason, we decided to consider as the final equilibration time for this experiment the kink at  $t_3 = 2.5 \times 10^5$  with no significant crystallization after this time (Fig. 5a).

The crystallization time ( $t_3$ ) strongly differs between the two experimental datasets on Stromboli (between  $4\text{--}5 \times 10^4$  s) and Etna (between  $4\text{--}25 \times 10^4$  s) (Table 2). For instance, samples SGP7 (Stromboli) and E92-1 (Etna) were run at similar undercooling conditions ( $\Delta T_0 = 22.8 \pm 2.2$  °C) yet achieved their viscosity plateaus at  $t_3 = 5 \times 10^4$  s and  $t_3 = 2.5 \times 10^5$  s, respectively. The higher crystallization time of sample E92-1 also results in a lower plagioclase crystal content ( $\phi = 0.06$ ) at the rheological equilibrium with respect to SGP7 ( $\phi = 0.11$ ) (Table 3). The same behavior can be observed by comparing samples SGP3 (Stromboli) and E92-2 (Etna), both run at  $\Delta T_0 = 45.9 \pm 0.4$  °C. The crystallization time of SGP3 is  $t_3 = 4 \times 10^4$  s, while it is  $t_3 = 16 \times 10^4$  s for E92-2. The resulting plagioclase crystal fractions are  $\phi = 0.17$  and  $\phi = 0.13$ , respectively.

## CSD analysis

### Crystal shape and size distributions

In this work, we investigated in detail shape and size distribution of the plagioclase phase, as it is the most abundant phase in all our experiments. Crystal habits were evaluated using the *CSDslice* software implemented by Morgan and

**Table 3** Results of CSD analysis

Run	Stromboli						Etna		
	SGP7	SGP5	SGP4	SGP1	SGP3	SGP6	E92-1	E92-2	E92-3
$\Delta T_0$ (plg) (°C)	25	30.2	35.3	40.4	45.5	55.8	20.6	46.3	72
$\phi_{\text{Plg}}$ (% vol) <sup>a</sup>	0.11	0.12	0.13	0.13	0.17	0.23	0.06	0.13	0.18
Area measured (mm <sup>2</sup> )	37.365	50.450	57.495	28.545	51.056	24.302	46.394	43.183	23.159
Number of Plg crystals	753	1,568	2,387	960	3,927	3,293	102	1,048	1,027
$\phi_{\text{Plg}}$ CSD (% vol) <sup>b</sup>	0.08 (0.02)	0.10 (0.02)	0.10 (0.02)	0.11 (0.02)	0.17 (0.02)	0.19 (0.02)	0.06 (0.02)	0.12 (0.02)	0.16 (0.02)
<i>Population <math>i_{\text{pop}}</math> (2D <math>l &gt; 100 \mu\text{m}</math>)</i>									
Intercept $\ln(n_0)$ (mm <sup>-4</sup> )	6.12 (0.21)	6.84 (0.15)	7.16 (0.12)	6.99 (0.19)	7.45 (0.12)	9.32 (0.11)	3.32 (0.23)	7.00 (0.15)	7.83 (0.12)
Slope (mm <sup>-1</sup> )	-6.72 (0.42)	-7.97 (0.35)	-9.19 (0.35)	-8.18 (0.47)	-8.65 (0.29)	-13.67 (0.40)	-3.48 (0.32)	-8.15 (0.36)	-9.64 (0.40)
<i>Population <math>q_{\text{pop}}</math> (2D <math>l &lt; 100 \mu\text{m}</math>)</i>									
Intercept $\ln(n_0)$ (mm <sup>-4</sup> )	8.65 (0.16)	9.22 (0.10)	10.35 (0.09)	10.20 (0.14)	10.64 (0.07)	11.91 (0.07)	4.88 (1.03)	8.76 (0.23)	11.67 (0.20)
Slope (mm <sup>-1</sup> )	-18.52 (0.70)	-19.28 (0.53)	-32.24 (0.70)	-29.59 (0.87)	-25.28 (0.47)	-34.14 (0.70)	-12.28 (1.69)	-17.51 (1.03)	-72.98 (1.4)

Numbers in brackets represent  $1\sigma$  standard deviation

<sup>a</sup> Plg crystal fraction calculated by image analysis

<sup>b</sup> Plg crystal fraction determined from CSDs using Eqs. (1–2)

Jerram (2006), which compares the distribution of 2D size measurements to a database of shape curves, determining through regression calculation a best-fit 3D crystal habit in terms of short (*S*), intermediate (*I*) and long (*L*) axis. Raw 2D crystal size measurements expressed as short and long axes of the best-fitting ellipse (2D intersection width *w*, and length *l*) were converted using *CSDslice* to 3D crystal habits (*S:I:L*) ranging between 1:2:10 and 1:3.4:10, with intermediate axis *I* slightly changing between different samples. On the basis of crystal shapes, 2D long axes of the best-fitting ellipse were converted to true three-dimensional crystal size distributions using *CSDCorrections* (Higgins 2000, 2006a, b). This program incorporates stereological corrections for the intersection probability effect (Underwood 1970; Royet 1991; Sahagian and Proussevitch 1998) and cut-section effect (Saltikov 1967; Armienti et al. 1994; Peterson 1996; Sahagian and Proussevitch 1998; Higgins 2000). The cut-section effect is related to the production of different-sized section of a grain depending on its orientation, whereas the intersection probability deals with the statistical problem of the higher probability of intersecting a large grain rather than a small one. The adopted size intervals (bins) are logarithmic with each bin being  $10^{0.2}$  larger than the next smallest bin. A logarithmic binning of size classes is recommended by several authors (e.g., Higgins 2006a, b; Armienti 2008) as it allows to reduce the effect of flattening of CSD at the limit of the distribution (right-hand truncation, RHT; Armienti 2008)

by increasing the number of crystals sampled for each bin at large sizes.

Figure 6 shows CSD diagrams for the plagioclase phase for both Stromboli (a) and Etna (b). CSD diagrams are semi-logarithmic and display the population density,  $n(L)$  (mm<sup>-4</sup>) that is the number of crystals of given size *L* contained in the unit volume versus a characteristic length (*L*) of the grains (Randolph and Larson 1971; Marsh 1988; Cashman and Marsh 1988). All the distributions present the same general concave-up shape. The downturn toward the small sizes if present (as for instance in the distribution of sample E92-2, Fig. 6b) is most likely an artifact derived from image resolution (left-hand truncation, LHT; Armienti 2008). In fact, the spatial resolution of the images set the lowest measurable size at around 4  $\mu\text{m}$  and the downturn seems to disappear for larger sizes. Following Higgins (2002), to verify that CSDs have been correctly converted from two-dimensional data, we compared the values of the plagioclase phase content measured by direct image analysis with those calculated by the CSD. Plagioclase volume fraction can in fact be calculated by CSD as follows:

$$V_i = \sigma \sum n_i (\bar{L}_j) \bar{L}_j^3 W_j \quad (1)$$

where  $\sigma$  is a shape factor, *n* is the population density, *j* is the number of intervals,  $W_j$  is the width of the interval, and  $\bar{L}_j$  is the mean size of the interval *j*. The shape factor  $\sigma$  is equal to:

$$\sigma = [1 - \Omega(1 - \pi/6)]IS/L^2 \quad (2)$$

where  $\Omega$  is the roundness factor, which varies from 0 for rectangular parallelepipeds to 1 for a triaxial ellipsoid.  $S$ ,  $I$  and  $L$  are the average short, intermediate and long dimensions of the crystals. Based on the observation of crystal shapes in thin sections (Fig. 4), we adopted  $\Omega = 0.1$ . The very good correlation between the actual volumetric phase proportion and that determined from the CSD using Eqs. (1–2) (Table 3) indicates that the CSDs have been correctly determined from 2D measurements.

#### Interpretation of CSDs

Many attempts have been made to explain curvature in the CSDs of natural magmas (e.g., Armienti et al. 1994; Bindeman 2003; Higgins 1996a, 1998, 2002; Higgins and Roberge

2003; Marsh 1998; Zieg and Marsh 2002) by changes in the magma cooling rate, crystal aggregation, textural coarsening and magma mixing. In our case, interpretation of the CSD curves is facilitated by the known cooling history of the samples. It is well known that a change in physical or chemical conditions affects crystallization parameters (e.g., nucleation and growth rate), which in turn will reflect in changes of CSDs shape. Curved CSDs have often been interpreted in the literature as due to mixing of different populations of crystals formed at different thermal regimes (for instance in the magma chamber, during ascent along a conduit, during quenching in air) where each linear segment pertains to a different population of crystal (Cashman and Marsh 1988; Armienti et al. 1994; Piochi et al. 2005; Salisbury et al. 2008; Higgins 1996b). Considering the type of experiments performed in this study, the concave-up trend shown in our CSDs can derive from the disequilibrium conditions given by the

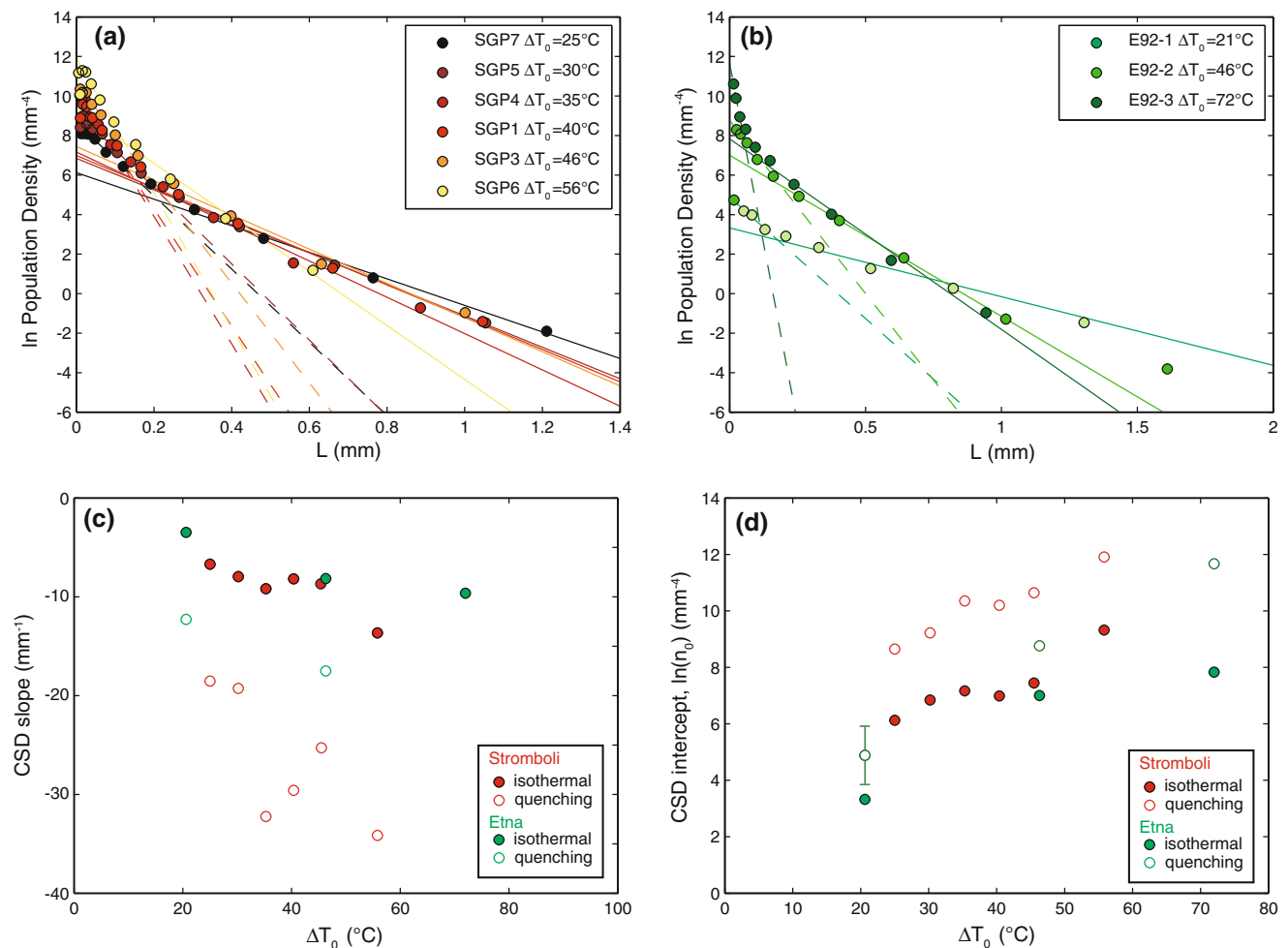


**Fig. 6** Crystal size distributions analysis. **a–b** CSDs calculated using *CSDCorrections* (Higgins 2000) for Stromboli (**a**) and Etna (**b**) samples. The segments pertaining to “quenching population” ( $q_{\text{pop}}$ ) and “isothermal population” ( $i_{\text{pop}}$ ) were each linearly fitted with a cut-off size of approximately 100  $\mu\text{m}$ . The results of fittings are displayed as solid ( $i_{\text{pop}}$ ) and dashed ( $q_{\text{pop}}$ ) lines. **c–d** Slopes (**c**) and intercepts

(**d**) obtained by linear regression of CSD data in (**a–b**) as a function of undercooling  $\Delta T_0$ . In **c**, the value relative to E92-3  $q_{\text{pop}}$  ( $\Delta T_0 = 72^\circ\text{C}$ ; Slope =  $-73 \text{ mm}^{-1}$ ) has been omitted to optimize visualization of isothermal population parameters; if not displayed, error bars are within the symbols



rapid, strong thermal perturbation undergone by the magma during quenching. In this case, we expect a CSD formed by a combination of a steep slope at small sizes (produced by quenching crystals) and a more gentle slope at larger sizes (formed by crystals generated during the main experimental stage). These two different segments pertaining to the different populations of crystals [termed “quenching population” ( $q_{\text{pop}}$ ) and “isothermal population” ( $i_{\text{pop}}$ )] were fitted separately, with a cut-off size of approximately 100  $\mu\text{m}$  (2D value before stereological correction).

Both populations were fitted to a linear equation of the form:  $\ln(n) = \ln(n_0) + s \times L$ , where  $\ln(n_0)$  and  $s$  are the intercept and the slope of the linear approximation, and  $n_0$  represents a measure of the crystal population at vanishing size (nucleation density; Marsh 2007). Log-linear fittings are shown in Fig. 6a, b, and the results of the regression are reported in Fig. 6c, d as a function of undercooling and in Table 3. Isothermal population ( $i_{\text{pop}}$ ) curves slightly sharpen with decreasing experimental temperature with slopes  $s$  decreasing (i.e., increasingly more negative) from  $-6.72$  to  $-13.67 \text{ mm}^{-1}$  for Stromboli and from  $-3.48$  to  $-9.64 \text{ mm}^{-1}$  for Etna. Furthermore, an increase in the intercept,  $\ln(n_0)$ , with decreasing  $T$  has been observed from  $6.12$  to  $9.32 \text{ mm}^{-4}$  and from  $3.32$  to  $7.83 \text{ mm}^{-4}$  for Stromboli and Etna, respectively. As for quenching population ( $q_{\text{pop}}$ ), the fitted curves are steeper than  $i_{\text{pop}}$  curves, displaying the same general trend with slopes decreasing from  $-18.52$  to  $-34.14 \text{ mm}^{-1}$  for Stromboli and from  $-12.28$  to  $-72.98 \text{ mm}^{-1}$  for Etna, and intercepts increasing from  $8.65$  to  $11.91 \text{ mm}^{-4}$  for Stromboli and from  $4.88$  to  $11.67 \text{ mm}^{-4}$  for Etna.

Within a single series, the combination of increasing intercept and decreasing slope with increasing undercooling yields crystal size distributions progressively steeper at lower temperatures. The resulting “fanning” behavior has been commonly observed in natural samples (e.g., Zieg and Marsh 2002) and it is usually interpreted as the result of increasing cooling rate through time in accordance with the thermal regime, with fast cooling producing steeper CSDs. Our experiments were conducted at isothermal conditions, so variation of cooling rates cannot be advocated directly as the cause of such behavior. However, increasing undercooling (from 25 to 56  $^{\circ}\text{C}$  for Stromboli and from 21 to 72  $^{\circ}\text{C}$  for Etna) can mimic varying cooling rates conditions giving rise to similar variations in the CSDs trends.

## Discussion

Effects of undercooling and deformation rates on crystallization kinetics

Stromboli and Etna magmas are characterized by very similar chemical compositions (Table 1) and *liquidus* temperatures

( $T = 1,248$  and  $1,251$   $^{\circ}\text{C}$  for Stromboli and Etna, respectively), according to MELTS calculations (Ghiorso and Sack 1995; Asimow and Ghiorso 1998). The post-run samples reflect this similarity showing the same mineralogical assemblage, constituted by spinel + plagioclase  $\pm$  clinopyroxene (only at the lowest temperatures; Fig. 4). The observed differences in the time needed to achieve “rheological equilibrium” and the final crystal content as a function of the undercooling may be attributed mainly to different stirring conditions.

As reported in previous studies (e.g., Uhlmann et al. 1977; Tsuchiyama 1983), the delay in nucleation (the time required until nucleation takes place, or incubation time) decreases with increasing  $\Delta T$ . Moreover, it is strongly affected by the presence of flow, decreasing with increasing deformation rate (Kouchi et al. 1986). This behavior can be observed from the viscosity-time paths in Fig. 1 by focusing on the first horizontal section of the curves ( $t_1$ – $t_2$  in Fig. 1a; Table 2). These horizontal sections can be interpreted as the viscosity of a metastable liquid, before crystallization takes place. Although it is not possible to quantify exactly the incubation time, as the first crystal nuclei could yield no appreciable variation of the viscosity of the melt, a reduction in the length of horizontal sections of the curves can be observed both with increasing undercooling within a single dataset (Stromboli and Etna) and with increasing deformation rate by comparing the two datasets.

In Fig. 7, the final plagioclase contents are reported as a function of undercooling. Both datasets on Stromboli and Etna show a linear trend that can be fitted by linear regression. Within each single series, crystal content

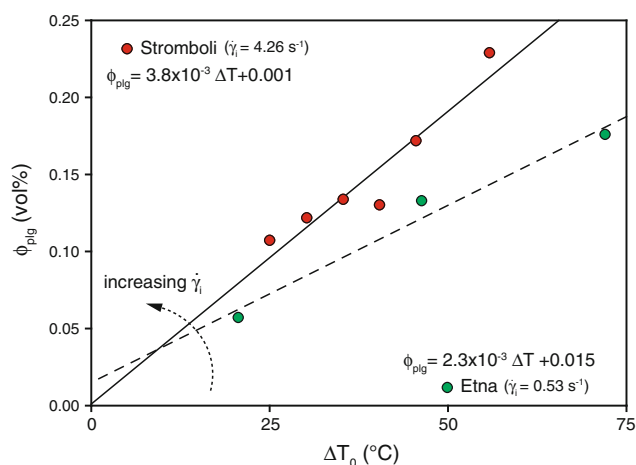


**Fig. 7** Plagioclase volume fraction against undercooling for Stromboli (green) and Etna (red). Solid (Stromboli) and dashed (Etna) lines represent linear regressions according to the equations reported in the diagram ( $R^2 = 0.90$  and  $0.98$ ). The initial strain rates ( $\dot{\gamma}$ ) for the two datasets are reported. Increasing  $\dot{\gamma}$  yields a steeper slope

continuously increases as a function of undercooling. Extrapolated to zero undercooling, both lines converge to zero, indicating a good agreement between the temperature values for the onset of plagioclase crystallization calculated by MELTS and those occurring in our experiments. However, with increasing degree of undercooling ( $\Delta T \geq 50$  °C), the trends diverge with Stromboli data displaying a steeper slope with respect to Etna, hence reaching a higher crystal content at similar degrees of undercooling. Such a divergence can be explained by the different kinetics of the crystallization process in the two sets of experiments. As previously stated, the main difference between the two sets of experiments resides in the different stirring conditions for Stromboli and Etna basalts. The mechanical movement of magma during crystallization has been suggested to strongly favor nucleation density and decrease at the same time the incubation time (Kouchi et al. 1986). In the steady-state nucleation theory, nucleation rate is given by (Toshev 1973):

$$J = KD^* \exp(-\Delta G^*/kT) \quad (3)$$

where  $D^*$  is the diffusional transport,  $\Delta G^*$  the activation energy,  $k$  the Boltzmann's constant and  $K$  a constant. The increase in nucleation rate and nucleation density due to stirring conditions, which may approximate deformation of a magma during its ascent along a conduit or movement along a lava flow, can be attributed to convective transportation of matter which yield larger values of the transport factor  $D^*$ , compared to static conditions (Kouchi et al. 1986). In this framework, the decrease in incubation time for Stromboli experiments compared to Etna experiments can be explained by more rapid stirring conditions providing a greater availability of matter for the subcritical nucleus to be stabilized. Growth could also be facilitated by the flow of the magma, allowing a more efficient transport of fertile liquid near the liquid-surface interface (Higgins 1996b). This process could overcome the contrasting effect of increasing liquid viscosity as  $\Delta T$  increases, in hindering atomic diffusion and thus limiting both nucleation and growth. Therefore, on Stromboli samples, the stirring-aided nucleation and growth processes would permit, within the experimental time, the achievement of equilibrium crystal content (as testified by the good match between measured plagioclase amounts and those calculated by MELTS). In contrast, for Etna, the occurrence of a slow, diffusion-limited growth would limit the achievement of the equilibrium amount of crystals in the experimental time-span, as highlighted by the discrepancy between MELTS calculation and measured crystal content. From the final crystal content and the incubation time as derived from the viscosity versus time curve, we therefore infer both the nucleation and growth are higher than in normal static experiments.

## Nucleation and growth rates

CSDs are commonly used to decipher the kinetics of crystallization of magmas (Cashman and Marsh 1988; Marsh 1988; Armienti 2008). In this study, we observe two segments each with log-linear distributions with increasing size (Fig. 6). The straight lines from each dataset (Stromboli and Etna) on the CSD diagram define a fan as a function of undercooling, with steeper CSDs pertaining to higher undercoolings. As discussed by Marsh (1998), the common log-linear decrease in population density as a function of crystal size can be explained, in a closed system under constant cooling rate conditions, by two end-member scenarios. Either (1) nucleation rate  $J$  increases exponentially as a function of time with constant growth rate  $G$  or (2) growth rate  $G$  increases exponentially as a function of crystal size, nucleation rate being constant. The first model has been widely adopted for modeling crystallization kinetics as a function of different cooling rates (e.g., Zieg and Lofgren 2006; Resmini 2007; Armienti 2008; Blundy and Cashman 2008; Pupier et al. 2008). Our experiments differ from the constant cooling rate experiments described above, as they are performed at constant undercooling conditions. In this case, as the crystallization proceeds, the effective undercooling related to the residual liquids is bound to decrease until equilibrium conditions are reached. As equilibrium conditions are approached, growth and nucleation rates of crystals tend to zero, unlike the case described above for constant cooling rate batch (closed system) experiments, and this will affect number density and CSD shape. Moreover, in a batch system, constant undercooling (before thermal equilibration takes place) should yield constant nucleation rate with number of crystals increasing linearly with time. If the growth rate is also the same for all crystals, then the crystals formed at the same time should have the same size at the end of the experiment. Since the nucleation rate is constant, the population density should also be constant, and the CSDs should display a horizontal line in the semi-logarithmic diagram (Maaloe et al. 1989). For the last part of the experiments, continuous decreasing of  $J$  and  $G$  would be expected, resulting in a positive slope of the CSDs. The real CSD shape of our experiments is clearly totally different from what expected (Fig. 6).

In general, mixing of different population of crystals formed at different cooling rates would yield segmented CSD with each linear segment pertaining to a different population of crystals (Higgins 1996b). Considering the type of experiments performed in this study, the CSDs formed by a combination of a steep slope at small size and a more gentle slope at larger sizes can be considered as the sum of two populations of crystals, namely the quenched crystals (steep slope at small size) and crystals generated

during the main experimental stage (more gentle slope at larger size). In this framework, the positive slope at small sizes, which should be produced by the continuous decrease of  $G$  and  $J$  during the attainment of equilibrium conditions, could be masked by the presence of quench crystals. The slope pertaining to crystals generated during the main experimental stage should still, according to the model presented above, be horizontal. Agglomeration and coarsening of middle-sized crystals together with growth rims around preexisting crystals during quenching could be responsible for the observed slope (Voorhees 1992; Higgins 1998; Bindeman 2003; Pupier et al. 2008). Downturn toward small sizes which usually accompanies agglomeration and coarsening would be also in this case masked by quench crystals. Since  $G$  cannot be considered constant as a function of time and/or size, this precludes the use of the CSD trends to extract reasonable kinetic parameters.

$G$  and  $J$  calculations were therefore performed only in relation to the main experimental stage, therefore not including the quenched crystal, through the following approaches. In a batch system, the simplest way to calculate maximum growth rates is from the size of the largest crystals found in the experimental products (Walker et al. 1976; Gardner et al. 1998; Marsh 1998; Hammer and Rutherford 2002). Following a method reported by Hammer and Rutherford (2002) and Couch (2003), the length ( $l$ ) and the width ( $w$ ) of the 10 largest crystals were measured and  $G$  values were the calculated using the formula:

$$G = (l \times w)^{0.5} / (2 \times \Delta t) \quad (4)$$

where  $\Delta t$  is the experimental time. The factor of 1/2 accounts for growth in two opposite directions away from the crystal center.

Average nucleation rates  $J$  can be calculated from 2D bulk population, by dividing the number of crystals by the experimental time (Hammer and Rutherford 2002; Couch et al. 2003; Larsen 2005; Blundy and Cashman 2008; Brugger and Hammer 2010):

$$J = N_V / \Delta t \quad (5)$$

where  $N_V$  is the volume number density. To calculate  $N_V$ , area number density ( $N_A$ ) and area fraction ( $\phi$ ) measurements are first used to calculate a characteristic crystal size ( $S_N$ ) as:

$$S_N = (\phi / N_A)^{0.5} \quad (6)$$

and then the volumetric number density  $N_V$  is given by:

$$N_V = N_A / S_N \quad (7)$$

We used Eqs. (5–7) to calculate average nucleation rates relative to the population of crystals with 2D length >100  $\mu\text{m}$ . By considering only 2D lengths higher than

100  $\mu\text{m}$ , we purposely excluded quench crystals from the calculation. It must be noted that the overall crystal content does not change significantly without the contribution of quench crystals, due to their extremely small sizes. In general, the crystal content calculated in both ways are within the error inherent to the determination of the crystal fractions by image analyses (less than 1–2 %).

#### Crystallization time at constant undercooling

As stated above, since our experiments are conducted at isothermal conditions, undercooling changes during equilibration leading to a variation in the kinetic parameters with time. In order to be able to associate a value of  $G$  and  $J$  at a known undercooling, we have to define the time–temperature interval where undercooling can be considered constant and equal to the initial imposed value (initial undercooling,  $\Delta T_0$ ). Normalized to this initial value, undercooling ( $\Delta T$ ) can be expressed through the solid fraction with a linear approximation as

$$\Delta T(t) / \Delta T_0 = 1 - \alpha \phi \quad (8)$$

where  $\phi$  (i.e., the volumetric fraction of crystals) for any time  $t > 0$  can be expressed as follows:

$$\phi(t) = c \int_0^t J(\Delta T(t - \tau)) \left( \int_{t-\tau}^t G(\tau) d\tau \right)^k d\tau, \quad k = 2 \div 3, \quad (9)$$

where  $J$  and  $G$  are nucleation and growth rates, respectively,  $\Delta T$  is the undercooling, and the value of  $k$  depends on the crystal shape ( $k = 3$  for isometric crystals) (Avrami 1939, 1940; Lasaga 1998; Marsh 1988; Spillar and Dolejs 2013).

In general, the shape of the  $G(\Delta T)$  dependence is a function of the crystallizing system, differing strongly in the case of crystals growing from their own melts (e.g., Di, Kirkpatrick 1976), or in the case of solid solutions (Ab–An, Muncill and Lasaga 1988) or with eutectic-type melts (Fsp–Q, Simak and Chevychev 1995). In the latter case, the authors observed that crystal growth rates remain constant for a wide undercooling range, pertaining to moderate  $\Delta T$  values. If the experiments are conducted within this undercooling interval, like in the case of our experimental study, then Eq. (9) can be simplified by setting constant growth rate  $G_0$  and variable  $J(\Delta T)$ :

$$\Delta T(t) / \Delta T_0 = 1 - b \int_0^t J(\Delta T(t - \tau)) (G_0 \tau)^3 d\tau \quad (10)$$

Nucleation rate can be expressed as function of the undercooling with the following expression, valid for small

to intermediate undercooling range (e.g., Kirkpatrick 1975; Swanson 1977):

$$J = A \exp(-b_1/\Delta T^2) \quad (11)$$

From this general relation, it follows that there is a threshold undercooling for the homogeneous nucleation to occur, and after this threshold, nucleation rate increases very rapidly with undercooling. For undercoolings lower than those producing maximum nucleation rates, we can approximate Eq. (11), assuming  $J$  proportional to the cube of  $\Delta T$  (i.e.,  $J \propto \Delta T^3$ ), and substitute this expression in Eq. (10). With all the assumptions expressed above, Eq. (10) becomes an integral equation relative to the unknown function  $\Delta T(t)$  and can be solved by successive iterations method:

$$\Delta T_{k+1}(t)/\Delta T_0 = 1 - 6.0 \int_0^t \Delta T_k^3(t-\tau)\tau^3 d\tau, \quad k > 1 \quad (12)$$

We initially approximated the nucleation rate as  $J = Heaviside(\tau - t + 0.5)$ , that is constant nucleation operates in the first 0.5 time units and then it stops completely as the experiment reaches equilibrium conditions. With this first approximation ( $k = 1$ ), Eq. (12) becomes:

$$\Delta T_k(t)/\Delta T_0 = 1 - 6.0 \int_0^t Heaviside(\tau - t + 0.5)\tau^3 d\tau, \quad k = 1 \quad (13)$$

The solution of Eq. (12) converges on the second iteration, as it is shown in Fig. 8. As it can be observed,

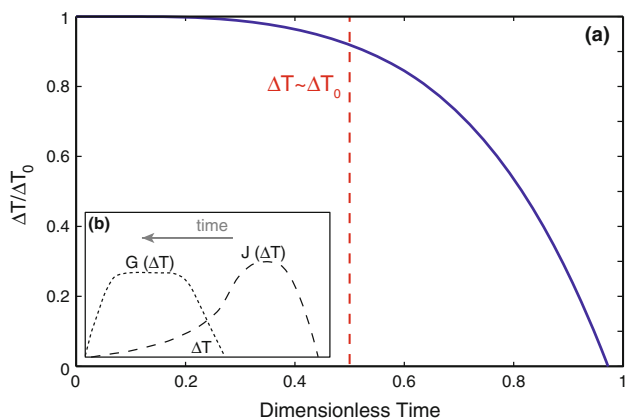


**Fig. 8** Results of calculation of undercooling-time evolution. **a** Blue line represent the solution of Eq. (12). As it can be seen, the undercooling  $\Delta T$  can be taken as constant and close to the initial undercooling ( $\Delta T_0$ ) only for the first 0.5 dimensionless time. **b** Theoretical shape of nucleation ( $J$ ) and growth rate ( $G$ ) as a function of  $\Delta T$ . Since with time  $\Delta T$  tends to zero, also  $J$  and  $G$  will tend to zero. Given its relatively flat peak shape,  $G$  can be considered constant at small to intermediate undercoolings (Simakin and Chevychelov 1995)

undercooling remains constant for approximately half of the equilibration time and then drops rapidly to zero, when equilibrium crystallization conditions are reached. When calculating growth rates, we can then distinguish between *maximum growth rates* (termed  $2G = 2^*G$ ), calculated considering half the experimental time ( $t_3/2$ , therefore under constant undercooling conditions), and *average growth rates* ( $G$ ), considering the entire experimental time ( $t_3$ , as growth rate will tend to zero when approaching equilibrium conditions) (Table 2).

Nucleation rates in the range of undercooling considered in this study will tend to decrease continuously throughout the experiment, rendering very complicated if not impossible to define maximum  $J$ . Average  $J$  are therefore calculated only with the method described in the previous section (i.e., using  $t_3$  time).

#### Comparison with literature data

The results of the calculations are reported in Table 4. In Fig. 9, the values of calculated  $G$  (and  $2G$ ) and  $J$  are reported as a function of undercooling. Growth and nucleation rates for Stromboli are generally greater than those for Etna. Stromboli average growth rates  $G$  display a relative small variation with undercooling ( $1.9\text{--}3.4 \times 10^{-9} \text{ m s}^{-1}$ ; Fig. 9a). On the other hand, a slight increase of  $G$  with decreasing temperature can be observed for Etna, from  $0.6 \times 10^{-9}$  to  $1.9 \times 10^{-9} \text{ m s}^{-1}$  (Table 4). All these values double if growth at constant undercooling ( $2G$ ) is considered. Average nucleation rates  $J$  continuously increase with undercooling from  $1.35 \times 10^6$  to  $9.47 \times 10^6 \text{ m}^{-3} \text{ s}^{-1}$  for Stromboli (Fig. 9b). As for Etna, nucleation rate has an extremely low value of  $3.63 \times 10^4 \text{ m}^{-3} \text{ s}^{-1}$  at the lowest undercooling experiment ( $\Delta T_0 = 20 \text{ }^\circ\text{C}$ ). With increasing undercooling, the nucleation rates increase continuously to values more comparable with those obtained on experiments on the Stromboli material (up to  $4.0 \times 10^6 \text{ m}^{-3} \text{ s}^{-1}$ ). Growth rates (either as  $G$  or  $2G$ ) obtained in this paper are generally one or two orders of magnitude higher compared to those obtained in the literature for equivalent undercooling conditions.

Cashman (1990) suggested that crystal growth rates under most magmatic cooling conditions are fairly uniform between  $10^{-12}$  and  $10^{-13} \text{ m s}^{-1}$ . Armienti et al. (1994), on the basis of the maximum linear dimensions of plagioclase crystals in several lavas collected at different times during the 1991–1993 Mt Etna eruption estimated  $G = 2.4 \times 10^{-11} \text{ m s}^{-1}$  for olivine and  $7.1 \times 10^{-11} \text{ m s}^{-1}$  for plagioclase. Moreover, Armienti et al. (2007) provide even lower values for Stromboli natural magmas. In fact, from CSD analysis of historical eruptions, the authors found a plagioclase net growth rate of  $2 \times 10^{-13} \text{ m s}^{-1}$  resulting from a balance of growth ( $10^{-12} \text{ m s}^{-1}$ ) and resorption

**Table 4** Results of kinetic parameters calculations

Run	Stromboli						Etna		
	SGP7	SGP5	SGP4	SGP1	SGP3	SGP6	E92-1	E92-2	E92-3
Growth rates, $G$ ( $\text{m s}^{-1}$ )	2.16E-09 (0.16)	1.90E-09 (0.08)	3.35E-09 (0.28)	2.16E-09 (0.41)	2.62E-09 (0.13)	2.20E-09 (0.56)	5.77E-10 (0.17)	7.42E-10 (0.33)	1.85E-09 (0.20)
Nucleation rates, $J$ ( $\text{m}^{-3} \text{s}^{-1}$ )	1.35E+06 (0.20)	2.37E+06 (0.20)	4.10E+06 (0.20)	3.54E+06 (0.20)	7.09E+06 (0.20)	9.47E+06 (0.60)	3.63E+04 (0.20)	7.09E+05 (0.20)	3.98E+06 (0.20)

Numbers in brackets represent relative errors (%)

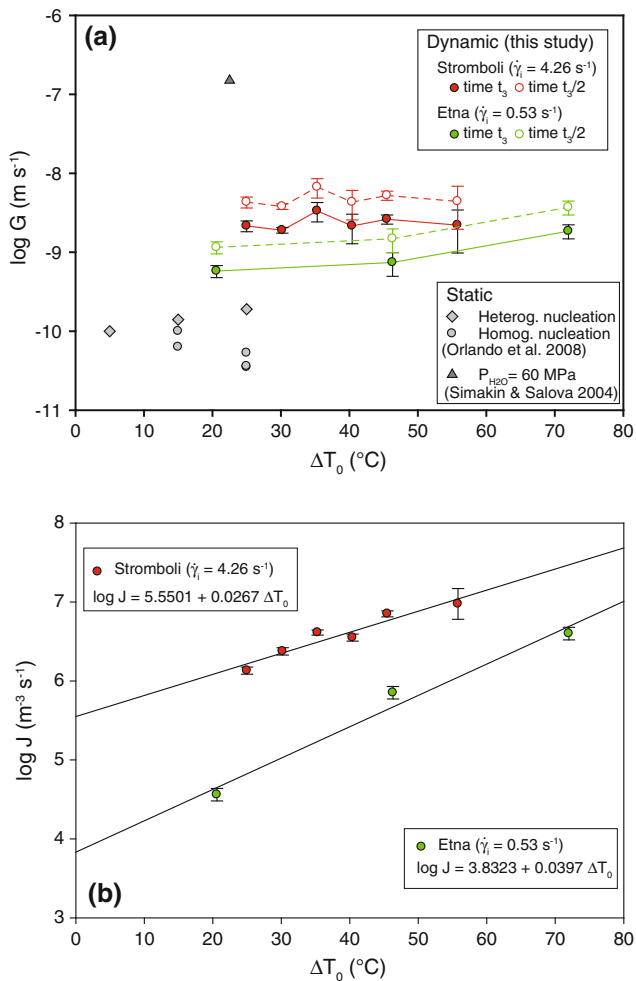


**Fig. 9** Rates of plagioclase growth and nucleation rates as function of undercooling. **a** Growth rates versus  $\Delta T$ . Growth rates ( $G$ ; full symbols), calculated using  $t_3$  as crystallization time, display a small variation with varying  $\Delta T$  for Stromboli (red), while a slight increase can be observed for Etna (green). If calculated at constant undercooling ( $2G$ ; empty symbols), by adopting  $t_3/2$  as crystallization time, a general shift toward higher values can be observed in both datasets (see text). Static crystallization experiments from Orlando et al. (2008) and Simakin and Salova (2004) are also reported for comparison. **b** Nucleation rates versus  $\Delta T$ . Both Stromboli (red) and Etna (red) data show increasing nucleation rate  $J$  with increasing  $\Delta T$ . Data are fitted to an equation of the form:  $\log(J) = \log(J_0) + a\Delta T_0$ . Fitting curves (black lines) and parameters are reported in the diagram

episodes on crystals larger than  $60 \mu\text{m}$  (deep-seated storage). Larsen (2005) obtained experimental growth rate in the order of  $10^{-11}$ – $10^{-12} \text{ m s}^{-1}$  for plagioclase crystals in a rhyodacitic  $\text{H}_2\text{O}$ -saturated melt at 50–150 MPa and  $\Delta T$ 's similar to those of our study. Similar or even lower values for  $G$  ( $10^{-11}$ – $10^{-13} \text{ m s}^{-1}$ ) were obtained for plagioclase and clinopyroxenes in magmas of different compositions (Kirkpatrick 1977; Cashman and Marsh 1988; Resmini and Marsh 1995; Turner et al. 2003). Higher  $G$  and  $J$  values than those typically reported in the literature were obtained by Pupier et al. (2008) from CSD data for plagioclase in basaltic magmas at different cooling rates and different *superliquidus* dwell times. For cooling rates between 0.2 and  $3 \text{ }^{\circ}\text{C/h}$ , the authors estimate  $J$  values between  $1 \times 10^7$  and  $1.3 \times 10^{10} \text{ m}^{-3} \text{s}^{-1}$  and  $G$  values calculated from CSD parameters between  $6 \times 10^{-11}$  and  $3.3 \times 10^{-10} \text{ m s}^{-1}$ . Maximum  $G$  values derived from largest crystal sizes vary from  $3.3 \times 10^{-10}$  to  $1.78 \times 10^{-9} \text{ m s}^{-1}$ . Those values are generally higher than those reported in the literature both for cooling and for isothermal experiments. The authors interpret this discrepancy as a result of a combination of heterogeneous nucleation, as their experiments were pre-heated at very low *superliquidus* conditions and very high cooling rates, which favor rapid crystal growth. Another recent set of studies, however, have found that microlite growth rates may be as high as  $10^{-10}$ – $10^{-9} \text{ m s}^{-1}$ . In these studies, experiments were performed to simulate ascending magmas conditions where crystallization is driven by decompression and water exsolution (Geschwind and Rutherford 1995; Gardner et al. 1998; Hammer et al. 1999; Couch et al. 2003).

Therefore, considering experimental studies performed both in isobaric and in polybaric conditions, plagioclase growth rates may vary over five orders of magnitude (Brugger and Hammer 2010). What is the rationale behind this large variation and how can we use growth rates to provide insight into magma crystallization kinetics during transport ascent and eruption conditions? In order to understand the best way to calculate magmatic timescales and to fully appreciate the effect of different physical conditions during the rising of magma along the conduit or during surface flow, we compare our results with the study

of Orlando et al. (2008) and the study of Simakin and Salova (2004).  $G$  values estimated for plagioclase crystal growth are reported for our study and Orlando et al. (2008) and Simakin and Salova (2004) in Fig. 9a.

Orlando et al. (2008) experimentally derived values of  $G$  for plagioclase and clinopyroxene for Etna basalt at degrees of undercooling similar to those explored in this study and in static conditions and atmospheric pressure. The authors measured both the plagioclase overgrowth rims on crystal seeds (heterogeneous nucleation) and the size of microlites (homogeneous nucleation). Their data indicate that  $G$  decreases from  $2 \times 10^{-10}$  to  $4 \times 10^{-11}$  m s<sup>-1</sup> with increasing undercooling, with the highest values pertaining to heterogeneous nucleation overgrowth rims.

The nucleation and growth rates obtained in this study pertain to homogeneous nucleation at constant temperature under flow conditions. The experiments were run on anhydrous basaltic magmas at atmospheric pressure and, similarly to the study of Orlando et al. (2008), can be applied to a near-surface ascending and degassing magma. Our experimental values are one or two orders of magnitude higher than Orlando et al. (2008) values. The reason for this apparent discrepancy resides in the different deformation regimes of these studies. Our experimental study was conducted using a stirring technique which simulates flow or convective conditions. The effect of stirring, through mechanical transport of matter, is to facilitate nucleation and growth of crystals resulting in the higher  $J$  and  $G$  observed.

However, both sets of data are visibly lower than those of Simakin and Salova (2004), who performed crystallization experiments from Etna at 60 MPa, under conditions close to water saturation and NNO-buffered oxygen fugacity and found that the plagioclase crystals appear at  $T = 1,170 \pm 5$  °C. These authors estimated  $G$  for plagioclase to be  $\sim 1.5 \times 10^{-7}$  m s<sup>-1</sup> at  $\Delta T$  of 10–15 °C and suggested that such high values of  $G$  should control CSD for crystal sizes smaller than 500 μm, when crystallization is coupled with degassing during magma ascent to the surface. The growth rates values reported by Simakin and Salova (2004) are in good agreement with the values reported by Geschwind and Rutherford (1995), Gardner et al. (1998), Hammer et al. (1999) and Couch et al. (2003), which are also related to ascending magmas conditions where crystallization is enhanced by decompression, water exsolution and rapid spontaneous crystallization as the magma becomes strongly undercooled. From this comparison, it is evident that, in order to interpret correctly the textural data and growth rates, it is of paramount importance to be able to define the physical environment where the data should be applied. Pressure conditions and water content of the magma seem to be first-order factors in

influencing kinetic parameters, as growth rates may vary several orders of magnitude during ascent and degassing of magmas along a conduit. Another critical parameter to be considered is convection inside the magma. Both under polybaric and isobaric conditions, convection strongly enhances crystal nucleation and growth. Results from this study indicate that next to the surface, when magma is degassed, at high oxygen fugacity,  $G$  for plagioclase is  $\sim 1$ –2 orders of magnitude lower than that obtained by Simakin and Salova (2004) at similar degrees of undercooling but 1–2 orders of magnitude higher than those reported by Orlando et al. (2008) performed in static conditions.

### Volcanological implications

Studies of crystal textures may provide many insight into magma crystallization kinetics. Historically, textural and CSD studies have been applied to the determination of crystal growth mechanisms, magma cooling rates, timing of magma mixing events, polybaric crystallization, crystal settling and timescales of magma ascent or magma residence time in a magma chamber (Armienti et al. 1994; Garrido et al. 2001; Bindeman 2003; Kile and Eberl 2003; Turner et al. 2003; Piochi et al. 2005; Brugger and Hammer 2010). It is very important for all those applications to consider appropriate thermal, barometric and rheological environment of the volcanological system under consideration.

Our 1 atmosphere kinetic experiments can be easily applied to lava flow conditions or cooling and crystallization in near-surface environments. As an example of the importance of stirring in influencing nucleation and crystal growth, we discuss the crystallization of a lava flow and possible transitions between pāhoehoe and ‘a‘ā lava flow morphologies. Basaltic lava flows can be classified as pāhoehoe or ‘a‘ā based on the dominant flow morphology. Generally speaking, pāhoehoe flow fields are fed by tube systems that allow lava transport over long distances with very little cooling, whereas ‘a‘ā flows develop when lava is transported through open channels, leading to rapid decrease in  $T$ , crystallization and rupture of the lava crust (Cashman et al. 1999). The morphologic and dynamic differences between the flow types can be mainly associated with different rheology of the flow interior and with the strength and thickness of the surface crust (Swanson 1973; Peterson and Tilling 1980; Kilburn 1981; Crisp et al. 1994; Cashman et al. 1999; Hon et al. 2003; Soule and Cashman 2005). Effusion rates, volcano slopes and initial temperature and viscosities are the most important parameters affecting the different rheologies. Usually the transitions between the two flow styles are attributed to

either (1) increasing apparent viscosity or (2) increasing strain rates (Peterson and Tilling 1980). In the first case, the change of the lava flow regime can be related to an increase in the effective viscosity of the flow interiors due to cooling, gas loss and increasing flow crystallinity (Cashman et al. 1999). In the second case, at constant crystal fraction, increasing shear rate induces strain localization culminating in the pāhoehoe–‘a‘ā transition (Soule and Cashman, 2005). Rather than acting independently, we have verified in our experimental study that an increase in strain rate also induces a simultaneous increase in viscosity via a faster crystallization kinetics. Our dynamic crystallization experiments allow us to describe the interplay between these two parameters and to model the transition between pāhoehoe and ‘a‘ā lava morphologies.

In this simulation, we have calculated, based on our experimental results, the crystallization-time paths of a basaltic lava flow under experimental strain rates ranging from 0.5 to 4.3 to s<sup>-1</sup>, typical of natural lava flow systems (Cashman et al. 1999; Soule and Cashman 2005). A cooling lava flow can be considered as the ideal batch system. According to the theory of crystal size distribution (Marsh 1988; Armienti 2008), in a batch system, the following relationship exists

$$n(t, L) = \frac{J(t_L)}{G(t_L)} \tag{14}$$

where *n* is the population density of crystals of size *L* at a specific time *t*, and *J* and *G* are the nucleation and growth rates at *t*. Crystal number density *n*(*L*) reflects the ratio *J*/*G* at the time in which crystals of size *L* appeared. The largest *L* reflects crystals first formed during cooling of the lava, whereas the smallest *L* reflects the last crystals to nucleate. In general, in a closed system under constant cooling rate conditions, the kinetic of crystallization can be modeled in the simplest case by nucleation rate *J* increasing exponentially as a function of time (and cooling) with constant growth rate *G* (Marsh 1998). In this framework, the increase in population density *n*(*t*, *L*) with decreasing crystal size (*L*) is due to the exponential increase of *J* with time (*J*(*t*)). We have simulated the cooling crystallization path for a basaltic lava flow deformed under strain rates of 0.5 s<sup>-1</sup> (based on kinetic data from experiments on Etna samples) and strain rates of 4.3 s<sup>-1</sup> (using data from Stromboli samples) (Table 5). We considered average growth rates from our experiments, 2*G* = 2.11 × 10<sup>-9</sup> m s<sup>-1</sup> and 2*G* = 4.79 × 10<sup>-9</sup>, respectively. In order to calculate *J*(*t*), we first fitted data in Fig. 9 with a simple exponential nucleation law: log(*J*) = log(*J*<sub>0</sub>) + *a* × Δ*T*. The results of fitting are reported in Table 5. We then considered two characteristic cooling rates of 0.01 and 0.001 °C s<sup>-1</sup> (Cashman et al. 1999; Harris and Rowland 2009). The fastest cooling rate (0.01 °C s<sup>-1</sup>) can be associated with

**Table 5** Parameters used for numerical simulation

Run	I	II	I	II
Strain rate (s <sup>-1</sup> )	4.26	4.26	0.53	0.53
Cooling rate (°C/s)	0.001	0.01	0.001	0.01
Average 2 <i>G</i> (m s <sup>-1</sup> )	4.79E-09	4.79E-09	2.11E-09	2.11E-09
Log <i>J</i> <sub>0</sub> (m <sup>-3</sup> s <sup>-1</sup> ) <sup>a</sup>	5.5501	5.5501	3.8323	3.8323
<i>a</i> <sup>a</sup>	0.0267	0.0267	0.0397	0.0397
<i>A</i> <sub>VFT</sub> <sup>b</sup>	-4.55	-4.55	-4.55	-4.55
<i>B</i> <sub>VFT</sub> <sup>b</sup>	5551	5551	5551	5551
<i>C</i> <sub>VFT</sub> <sup>b</sup>	603.5	603.5	603.5	603.5

<sup>a</sup> Parameters log *J*<sub>0</sub> and *a* are obtained from fitting data in Fig. 9b as: log *J* = log *J*<sub>0</sub> + *a*Δ*T*

<sup>b</sup> VFT parameters of the interstitial melt viscosity (log η = *A*<sub>VFT</sub> + *B*<sub>VFT</sub>/(*T* - *C*<sub>VFT</sub>)), calculated for Etna basalt using the model by Giordano et al. (2008b)

flows in open channels or with thin tube walls, while the slowest one to flows insulated by thick tube roofs (Harris and Rowland, 2009). The variation of nucleation rate with time *J*(*t*) can be derived based on the cooling rates chosen and the *J*(Δ*T*) relations. At this point, in order to simulate the crystallization-time path, the evolution of crystal number *n* and sizes *L* is calculated step by step with a time interval δ*t* following the method described in Pupier et al. (2008). The initial number of crystals is zero, and the initial melt volume is *V*<sub>0</sub>. For each time step, the number of crystals increases according to *J*(*t*) and the melt volume *V*(*t*):

$$n(t + \delta t) = n(t) + J(t) \times \delta t \times V(t) \tag{15}$$

The previously existing crystals grow according to the growth rate *G* such that for a given crystal *i*,

$$L_i(t + \delta t) = L_i(t) + G(L_i, t) \times \delta t \tag{16}$$

Overall crystal fraction at any time is then calculated as:

$$\phi(t) = \sum_i (X_i \times Y_i \times Z_i) \tag{17}$$

where *X*<sub>*i*</sub> is taken as *L*, and *Y*<sub>*i*</sub> and *Z*<sub>*i*</sub> are defined on the basis of the textural analyses as a constant ratio *X*:*Y*:*Z* = 1:3:10. The volume of residual melt decreases with increasing crystal fraction as:

$$V(t + \delta t) = V_0 - \phi(t) \tag{18}$$

Results of the modeling are reported in Table 5. Crystal fraction as a function of time is then reported in Fig. 10a. It should to be kept in mind that this exercise is based on a parameterization of *J* increasing exponentially with time and on the assumption that *G* is constant. Different behaviors of *G* and *J* as crystallization proceeds are not taken into account. Therefore, extrapolation at large crystal fraction (φ > 0.3–0.4) can be affected by systematic errors and it is not advised. Moreover, kinetic parameters adopted are related to

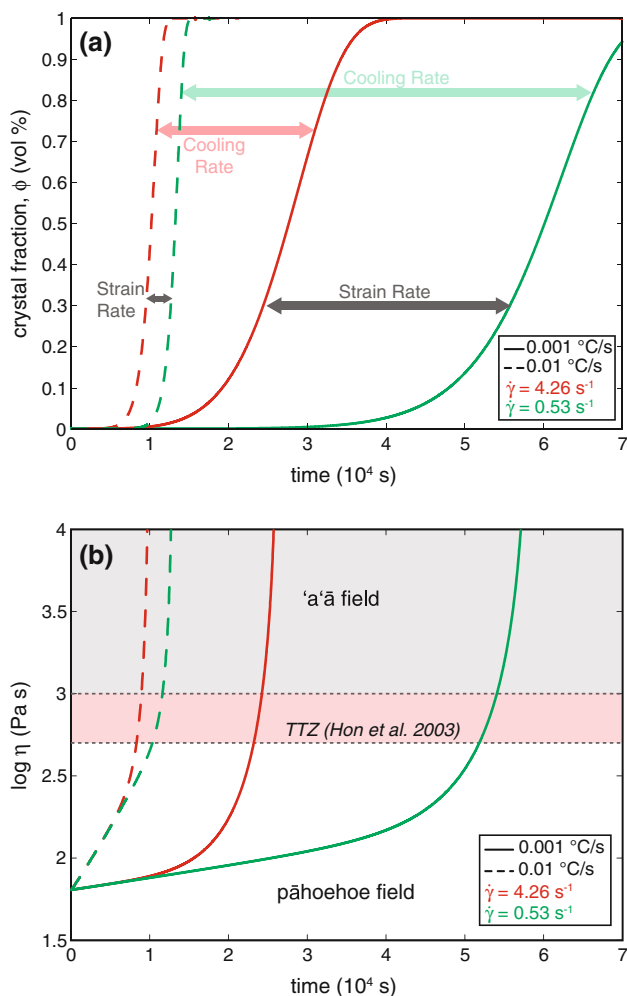


**Fig. 10** Numerical simulations of the crystallization-time path of a basaltic lava at different cooling rate (0.001–0.01 °C s $^{-1}$ ) and strain rate (4.26 and 0.53 s $^{-1}$ ). Red lines are high strain rate simulations (4.26 s $^{-1}$ ); green lines are low strain rate simulations (0.53 s $^{-1}$ ). Solid lines indicate high cooling rates (0.01 °C s $^{-1}$ ), dashed lines indicate slow cooling rates (0.001 °C s $^{-1}$ ). **a** Plagioclase crystal fraction ( $\phi$ ) as a function of time ( $t$ ). Horizontal arrows indicate the change in the parameter between the two curves. **b** Viscosity-time path for Stromboli and Etna, calculated according to the models of Giordano et al. (2008b) and Vona et al. (2011) considering Etna basalt composition and  $\phi(t)$  as from (a). The TTZ as defined by Hon et al. (2003) is reported, as a boundary between pahoehoe and 'a'a fields

homogeneous nucleation, while it is known that most basalts crystallize under conditions of heterogeneous nucleation on preexisting nuclei (Cashman 1993). Finally, initial temperature of the simulations corresponds to the plagioclase liquidus temperature ( $\Delta T_0 = 0$ ). Although the simplified assumptions considered in these simulations may not render the results immediately applicable to numerical simulation of lava flows, they are very important to visualize the effects of different physical environments on the crystallization kinetics and to determine the relative effects of the dynamic parameters investigated.

In all simulations, the crystal fraction increases exponentially as a function of time. As expected, within each series (high and low strain rate), the increase in crystal fraction with time is stronger for higher cooling rates, as a result of higher nucleation rate. The effect of strain rate on the crystallization kinetics can be evaluated by comparing simulations performed at the same cooling rate conditions. For instance, at fast cooling rate (0.01 °C/s), a crystal fraction of 30 % is obtained after  $9.5 \times 10^3$  and  $1.3 \times 10^4$  s for initial strain rates of 4.3 and 0.5 s $^{-1}$ , respectively. The effect of stirring is even more marked at lower cooling rates (0.001 °C/s), where the same crystal fraction is developed after  $2.4 \times 10^4$  and  $5.6 \times 10^4$  s for initial strain rates of 4.3 and 0.5 s $^{-1}$ , respectively.

In their semi-quantitative flow regime diagram, Hon et al. (2003) indicate a transition threshold zone (as defined by Peterson and Tilling 1980) in the shear strain rate–viscosity space between pahoehoe and 'a'a morphology. According to the authors, for Hawaiian lavas, this transition corresponds to viscosity of about 400–600 Pa s at 4 s $^{-1}$  and 500–1,000 at 0.5 s $^{-1}$ . To evaluate how the different crystallization-time patterns can influence the crossing of the boundary between pahoehoe and 'a'a morphology, we have calculated the time evolution of viscosity using prediction models available in the literature. The effects of temperature and crystallization on the rheology of the magmatic mixtures are reported in Fig. 10b. Liquid (crystal-free) viscosity has been calculated on chemical basis using the viscosity model by Giordano et al. (2008b). The Vogel–Fulcher–Tammann (VFT) expression [ $\log \eta = A_{VFT} + B_{VFT}/(T - C_{VFT})$ ] parameters are reported in Table 5. To facilitate the visualization of the simulation results, the calculations of liquid viscosity have been performed using Etna composition only. The viscosity of the suspensions (liquid + crystal) has been calculated according to the model of Vona et al. (2011), which considers the magma strain rate and both the crystal fraction and crystal shape factors. In fact, it is well known that beyond the crystal content, also the shape of crystals and in particular their anisotropy can influence dramatically the rheology of suspensions by increasing the chance to develop a crystal network at relatively low crystal content (e.g., Saar et al. 2001). In general, the rapid increase in crystal fraction with time translates to a fast increase in apparent viscosity (Fig. 10b). We assume a critical threshold viscosity value for the transition at  $\log_{10} \eta = 2.8$ – $3.0$ , representative of the transition threshold zone (TTZ) obtained by Hon et al. (2003). At fast cooling rates, the TTZ is crossed after  $0.8$ – $1.1 \times 10^4$  s (2–3 h), with the higher value pertaining to high strain rate. At low cooling rates, the TTZ is crossed after  $2.4 \times 10^4$  s (5.5 h) for high strain rates and after  $5.3 \times 10^4$  s (14.5 h) for low strain rates. It is evident from the simulations that the effect of



stirring is much more relevant at low cooling rates (i.e., for well-developed tube lava flows).

All other parameters being similar (i.e., melt viscosity and cooling rate), the difference in crystal fraction with time can be ascribed uniquely to the effect of stirring (which enhances both  $J$  and  $G$ ). Lava flow styles and transition between pāhoehoe and ‘a‘ā types are usually ascribed to differences in rheological regimes. Dynamic crystallization under different strain rates needs to be taken into account in order to define the rheological regimes and to model basaltic lavas flows and their transition from one flow regime to another.

## Conclusions

The effects of the degree of undercooling and deformation rates on the crystallization kinetics of plagioclase have been determined for Stromboli and Etna basalts through isothermal crystallization experiments. The results reveal that both degree of undercooling and deformation rate strongly control the kinetics of the crystallization process. With increasing undercooling and flow, a decrease in nucleation incubation time and an increase in nucleation density are observed. In addition, the flow of magma allows a more efficient transport of matter near the liquid–crystal interface, hence facilitating crystal growth. The nucleation and growth rates calculated are generally higher, up to one or two orders of magnitude, compared to those obtained in the literature for equivalent undercooling and static conditions. Higher growth and nucleation rates will lead to a faster increase in crystal fraction with time and possible change in the rheological response of the magma. Transitions between different eruptive styles or flow mechanisms can occur in a shorter amount of time if deformation is taken into account. We remark that the effect of magma flow on the crystallization kinetics cannot be neglected in the modeling of magma transport processes.

**Acknowledgments** Crystallization experiments were carried out at LMU University of Munich. The authors are grateful to Don Dingwell for his hospitality and for supervising the rheological analyses. We wish to thank Daniele Giordano for his help and discussions during experimental work and Danilo Di Genova for providing Tg data and helpful suggestions. Constructive comments from the editor and two anonymous reviewers greatly improved the paper. We acknowledge the financial support by INGV-DPC V1 (2012–2013) and PRIN 2009H37M59 projects.

## References

- Armienti P (2008) Decryption of igneous rock textures: crystal size distribution tools. *Minerals Inclusions Volcan Process* 69: 623–649. doi:10.2138/rmg.2008.69.16
- Armienti P, Pareschi MT, Innocenti F, Pompilio M (1994) Effects of magma storage and ascent on the kinetics of crystal-growth—the case of the 1991–93 Mt Etna eruption. *Contrib Miner Petrol* 115:402–414
- Armienti P, Francalanci L, Landi P (2007) Textural effects of steady state behaviour of the Stromboli feeding system. *J Volcanol Geoth Res* 160:86–98. doi:10.1016/j.volgeores.2006.05.004
- Asimow PD, Ghiorso MS (1998) Algorithmic modifications extending MELTS to calculate subsolidus phase relations. *Am Mineral* 83:1127–1132
- Avrami M (1939) Kinetics of phase change I. *J Chem Phys* 7:1103–1112
- Avrami M (1940) Kinetics of phase change II. *J Chem Phys* 8:212–224
- Bindeman IN (2003) Crystal sizes in evolving silicic magma chambers. *Geology* 31:367–370
- Blundy J, Cashman KV (2008) Petrologic reconstruction of magmatic system variables and processes. *Rev Mineral Geochem* 69:179–239. doi:10.2138/rmg.2008.69.6
- Brugger CR, Hammer JE (2010) Crystal size distribution analysis of plagioclase in experimentally decompressed hydrous rhyodacite magma. *Earth Planet Sci Lett* 300:246–254. doi:10.1016/j.epsl.2010.09.046
- Burkhard DJM (2002) Kinetics of crystallization: example of microcrystallization in basalt lava. *Contrib Miner Petrol* 142:724–737. doi:10.1007/s00410-001-0321-x
- Calvari S, Coltelli M, Neri M, Pompilio M, Scivano V (1994) The 1991–1993 Etna eruption: chronology and lava flow-field evolution. *Acta Vulcanol* 4:1–14
- Cashman KV (1990) Textural constraints on the kinetics of crystallization of igneous rocks. In: Nicholls J, Russell JK (eds) *Modern methods of igneous petrology: understanding magmatic processes*. *Rev Mineral Soc Am* 259–314
- Cashman KV (1993) Relationship between plagioclase crystallization and cooling rate in basaltic melts. *Contrib Miner Petrol* 113:126–142
- Cashman KV, Marsh BD (1988) Crystal size distribution (CSD) in rocks and the kinetics and dynamics of crystallization. II: Makaopuhi lava lake. *Contrib Miner Petrol* 99:292–305
- Cashman KV, Thornber C, Kauahikaua JP (1999) Cooling and crystallization of lava in open channels, and the transition of Pahoehoe Lava to ‘A‘a. *Bull Volcanol* 61:306–323
- Couch S (2003) Experimental investigation of crystallization kinetics in a haplogranite system. *Am Mineral* 88:1471–1485
- Couch S, Harford CL, Sparks RSJ, Carroll MR (2003) Experimental constraints on the conditions of formation of highly calcic plagioclase microlites at the Soufriere Hills Volcano, Montserrat. *J Petrol* 44:1455–1475
- Crisp J, Cashman KV, Bonini JA, Hougén SB, Pieri DC (1994) Crystallization history of the 1984 Mauna Loa lava flow. *J Geophys Res* 99:7177–7198. doi:10.1029/93JB02973
- Emerson OH (1926) The formation of aa and pahoehoe. *Am J Sci Ser* 5 V:109–114. doi:10.2475/ajs.s5-12.68.109
- Gardner CA, Cashman KV, Neal CA (1998) Tephra-fall deposits from the 1992 eruption of Crater Peak, Alaska: implications of clast textures for eruptive processes. *Bull Volcanol* 59:537–555. doi:10.1007/s004450050208
- Garrido CJ, Kelemen PB, Hirth G (2001) Variation of cooling rate with depth in lower crust formed at an oceanic spreading ridge: plagioclase crystal size distributions in gabbros from the Oman ophiolite. *Geochem Geophys Geosyst* 2:1041. doi:10.1029/2000GC000136
- Geschwind C-H, Rutherford MJ (1995) Crystallization of microlites during magma ascent: the fluid mechanics of 1980–1986 eruptions at Mount St Helens. *Bull Volcanol* 57:356–370. doi:10.1007/BF00301293

- Ghiorso MS, Sack RO (1995) Chemical mass transfer in magmatic processes IV. A revised and internally consistent thermodynamic model for the interpolation and extrapolation of liquid-solid equilibria in magmatic systems at elevated temperatures and pressures. *Contrib Miner Petrol* 119:197–212. doi:[10.1007/BF00307281](https://doi.org/10.1007/BF00307281)
- Giordano D, Potuzak M, Romano C, Dingwell DB, Nowak M (2008a) Viscosity and glass transition temperature of hydrous melts in the system  $\text{CaAl}_2\text{Si}_2\text{O}_8\text{--CaMgSi}_2\text{O}_6$ . *Chem Geol* 256:203–215. doi:[10.1016/j.chemgeo.2008.06.027](https://doi.org/10.1016/j.chemgeo.2008.06.027)
- Giordano D, Russell JK, Dingwell DB (2008b) Viscosity of magmatic liquids: a model. *Earth Planet Sci Lett* 271:123–134. doi:[10.1016/j.epsl.2008.03.038](https://doi.org/10.1016/j.epsl.2008.03.038)
- Hammer JE, Rutherford MJ (2002) An experimental study of the kinetics of decompression-induced crystallization in silicic melt. *J Geophys Res-Solid Earth* 107:2021. doi:[10.1029/2001jb000281](https://doi.org/10.1029/2001jb000281)
- Hammer JE, Cashman KV, Hoblitt RP, Newman S (1999) Degassing and microlite crystallization during pre-climactic events of the 1991 eruption of Mt. Pinatubo, Philippines. *Bull Volcanol* 60:355–380
- Harris AJL, Rowland SK (2009) Effusion rate controls on lava flow length and the role of heat loss: a review. In: Thordarson T, Self S, Larsen S, et al (eds) *Studies in volcanology: the legacy of George Walker*. Special Publications of IAVCEI, 2, Geological Society, London, pp 33–51
- Higgins MD (1996a) Magma dynamics beneath Kameni volcano, Thera, Greece, as revealed by crystal size and shape measurements. *J Volcanol Geoth Res* 70:37–48
- Higgins MD (1996b) Crystal size distributions and other quantitative textural measurements in lavas and tuff from Egmont volcano (Mt Taranaki), New Zealand. *Bull Volcanol* 58:194–204
- Higgins MD (1998) Origin of anorthosite by textural coarsening: quantitative measurements of a natural sequence of textural development. *J Petrol* 39:1307–1323
- Higgins MD (2000) Measurement of crystal size distributions. *Am Mineral* 85:1105–1116
- Higgins MD (2002) Closure in crystal size distributions (CSD), verification of CSD calculations, and the significance of CSD fans. *Am Mineral* 87:171–175
- Higgins MD (2006a) Verification of ideal semi-logarithmic, lognormal or fractal crystal size distributions from 2D datasets. *J Volcanol Geoth Res* 154:8–16. doi:[10.1016/j.jvolgeores.2005.09.015](https://doi.org/10.1016/j.jvolgeores.2005.09.015)
- Higgins MD (2006b) Quantitative textural measurements in igneous and metamorphic petrology. Cambridge University Press, Cambridge
- Higgins MD, Roberge J (2003) Crystal size distribution of plagioclase and amphibole from Soufriere Hills Volcano, Montserrat: evidence for dynamic crystallization-textural coarsening cycles. *J Petrol* 44:1401–1411
- Hon KA, Gansecki C, Kauhikaua J (2003) The transition from ‘a‘ā to pāhoehoe crust on flows emplaced during the Pu‘u ‘O‘o-Kupaianaha eruption. In: Heliker CA, Swanson DA, Takahashi TJ (eds) *The Pu‘u ‘O‘o-Kupaianaha eruption of Kilauea volcano, Hawai‘i: the first 20 years*. U.S. Geological Survey Professional Paper 1676, pp 89–104
- Iezzi G, Mollo S, Ventura G, Cavallo A, Romano C (2008) Experimental solidification of anhydrous latitic and trachytic melts at different cooling rates: the role of nucleation kinetics. *Chem Geol* 253:91–101. doi:[10.1016/j.chemgeo.2008.04.008](https://doi.org/10.1016/j.chemgeo.2008.04.008)
- Kilburn CRJ (1981) Pāhoehoe and ‘a‘ā lavas: a discussion and continuation of the model of Peterson and Tilling. *J Volcanol Geoth Res* 11:373–382
- Kile DE, Eberl DD (2003) On the origin of size-dependent and size-independent crystal growth: influence of advection and diffusion. *Am Mineral* 88:1514–1521
- Kirkpatrick RJ (1975) Crystal growth from the melt: a review. *Am Mineral* 60:798–814
- Kirkpatrick RJ (1976) Towards a kinetic model for the crystallization of magma bodies. *J Geophys Res* 81:2565–2572
- Kirkpatrick RJ (1977) Nucleation and growth of plagioclase, Makopuhi and Alae lava lakes, Kilauea Volcano, Hawaii. *Geol Soc Am Bull* 88:78–84
- Kouchi A, Tsuchiyama A, Sunagawa I (1986) Effect of stirring on crystallization kinetics of basalt: texture and element partitioning. *Contrib Miner Petrol* 93:429–438
- Landi P, Corsaro RA, Francalanci L, Civetta L, Miraglia L, Pompilio M, Tesoro R (2009) Magma dynamics during the 2007 Stromboli eruption (Aeolian Islands, Italy): mineralogical, geochemical and isotopic data. *J Volcanol Geoth Res* 182:255–268. doi:[10.1016/j.jvolgeores.2008.11.010](https://doi.org/10.1016/j.jvolgeores.2008.11.010)
- Larsen JF (2005) Experimental study of plagioclase rim growth around anorthite seed crystals in rhyodacitic melt. *Am Mineral* 90:417–427. doi:[10.2138/am.2005.1456](https://doi.org/10.2138/am.2005.1456)
- Lasaga AC (1998) *Kinetic theory in the earth sciences*. Princeton University Press, Princeton
- Lofgren GE (1974) An experimental study of plagioclase crystal morphology: isothermal crystallization. *Am J Sci* 274:243–273
- Lofgren GE (1980) Experimental studies on the dynamic crystallization of silicate melts. In: Hargraves RB (ed) *Physics of magmatic processes*. Princeton University Press, Princeton, pp 487–552
- Lofgren GE (1983) Effect of heterogeneous nucleation on basaltic textures: a dynamic crystallization study. *J Petrol* 24:229–255. doi:[10.1093/petrology/24.3.229](https://doi.org/10.1093/petrology/24.3.229)
- Maaloe S, Tumyr O, James D (1989) Population density and zoning of olivine phenocrysts in tholeiites from Kauai, Hawaii. *Contrib Miner Petrol* 101:176–186
- Macdonald GA (1953) Pāhoehoe, aa, and block lava. *Am J Sci* 251:169–191. doi:[10.2475/ajs.251.3.169](https://doi.org/10.2475/ajs.251.3.169)
- Marsh BD (1988) Crystal size distribution (CSD) in rocks and the kinetics and dynamics of crystallization I. Theory. *Contrib Miner Petrol* 99:277–291. doi:[10.1007/BF00375362](https://doi.org/10.1007/BF00375362)
- Marsh BD (1998) On the interpretation of crystal size distributions in magmatic systems. *J Petrol* 39:553–599
- Marsh BD (2007) Crystallization of silicate magmas deciphered using crystal size distributions. *J Am Ceram Soc* 90:746–757. doi:[10.1111/j.1551-2916.2006.01473.x](https://doi.org/10.1111/j.1551-2916.2006.01473.x)
- Morgan DJ, Jerram DA (2006) On estimating crystal shape for crystal size distribution analysis. *J Volcanol Geoth Res* 154:1–7. doi:[10.1016/j.jvolgeores.2005.09.016](https://doi.org/10.1016/j.jvolgeores.2005.09.016)
- Muncill GE, Lasaga AC (1988) Crystal-growth kinetics of plagioclase in igneous systems: isothermal H<sub>2</sub>O-saturated experiments and extension of a growth model to complex silicate melts. *Am Mineral* 73:982–992
- Orlando A, D’Orazio M, Armienti P, Borrini D (2008) Experimental determination of plagioclase and clinopyroxene crystal growth rates in an anhydrous trachybasalt from Mt Etna (Italy). *Eur J Mineral* 20:653–664. doi:[10.1127/0935-1221/2008/0020-1841](https://doi.org/10.1127/0935-1221/2008/0020-1841)
- Peterson TD (1996) A refined technique for measuring crystal size distributions in thin section. *Contrib Miner Petrol* 124:395–405
- Peterson DW, Tilling RI (1980) Transition of basaltic lava from pāhoehoe to ‘a‘ā, Kilauea Volcano, Hawaii: field observations and key factors. *J Volcanol Geothermal Res* 7
- Piochi M, Mastrolorenzo G, Pappalardo L (2005) Magma ascent and eruptive processes from textural and compositional features of Monte Nuovo pyroclastic products, Campi Flegrei, Italy. *Bull Volcanol* 67:663–678. doi:[10.1007/s00445-005-0410-1](https://doi.org/10.1007/s00445-005-0410-1)
- Pupier E, Duchene S, Toplis MJ (2008) Experimental quantification of plagioclase crystal size distribution during cooling of a basaltic liquid. *Contrib Miner Petrol* 155:555–570. doi:[10.1007/s00410-007-0258-9](https://doi.org/10.1007/s00410-007-0258-9)
- Randolph AD, Larson MA (1971) *Theory of particulate processes: analysis and techniques of continuous crystallization*. Academic Press, New York

- Resmini RG (2007) Modeling of crystal size distributions (CSDs) in sills. *J Volcanol Geoth Res* 161:118–130. doi:[10.1016/j.jvolgeores.2006.06.023](https://doi.org/10.1016/j.jvolgeores.2006.06.023)
- Resmini RG, Marsh BD (1995) Steady-state volcanism, paleoeffusion rates, and magma system volume inferred from plagioclase crystal size distributions in mafic lavas: Dome Mountain, Nevada. *J Volcanol Geoth Res* 68:273–296
- Royet J (1991) Stereology: a method for analyzing images. *Prog Neurobiol* 37:433–474. doi:[10.1016/0301-0082\(91\)90009-P](https://doi.org/10.1016/0301-0082(91)90009-P)
- Saar MO, Manga M, Cashman KV, Fremouw S (2001) Numerical models of the onset of yield strength in crystal-melt suspensions. *Earth Planet Sci Lett* 187:367–379
- Sahagian DL, Proussevitch AA (1998) 3D particle size distributions from 2D observations: stereology for natural applications. *J Volcanol Geoth Res* 84:173–196. doi:[10.1016/S0377-0273\(98\)00043-2](https://doi.org/10.1016/S0377-0273(98)00043-2)
- Salisbury MJ, Bohron WA, Clynne MA, Ramos FC, Hoskin P (2008) Multiple plagioclase crystal populations identified by crystal size distribution and in situ chemical data: implications for timescales of magma chamber processes associated with the 1915 eruption of Lassen Peak, CA. *J Petrol* 49:1755–1780. doi:[10.1093/ptology/egn045](https://doi.org/10.1093/ptology/egn045)
- Saltikov S (1967) The determination of the size distribution of particles in an opaque material from a measurement of the size distribution of their sections. In: Elias H (ed) *Proceedings of the second international congress for stereology*. Springer, Berlin, pp 163–173
- Sato H (1995) Textural difference between pahoehoe and aa lavas of Izu-Oshima volcano, Japan: an experimental study on population-density of plagioclase. *J Volcanol Geoth Res* 66:101–113
- Simakin AG, Chevychelov VY (1995) Experimental studies of feldspar crystallization from the granitic melt with various water-content. *Geohimia* 2:216–238
- Simakin AG, Salova TP (2004) Plagioclase crystallization from a Hawaiian melt in experiments and in volcanic conduit. *Petrology* 12:82–92
- Soule SA, Cashman KV (2005) Shear rate dependence of the pahoehoe-to-‘a’ā transition: analog experiments. *Geology* 33:361–364. doi:[10.1130/G21269.1](https://doi.org/10.1130/G21269.1)
- Spillar V, Dolejs D (2013) Calculation of time-dependent nucleation and growth rates from quantitative textural data: inversion of crystal size distribution. *J Petrol* 54:913–931. doi:[10.1093/ptology/egs091](https://doi.org/10.1093/ptology/egs091)
- Swanson DA (1973) Pahoehoe flows from the 1969–1971 Mauna Ulu Eruption, Kilauea Volcano, Hawaii. *Geol Soc Am Bull* 84:615–626. doi:[10.1130/0016-7606\(1973\)84<615:PFFTMU>2.0.CO;2](https://doi.org/10.1130/0016-7606(1973)84<615:PFFTMU>2.0.CO;2)
- Swanson SE (1977) Relation of nucleation and crystal-growth rate to the development of granitic textures. *Am Mineral* 62:966–978
- Toschev S (1973) Homogeneous nucleation. In: Hartman P (ed) *Crystal growth—an introduction*. Elsevier, New York, pp 1–49
- Tsuyuhama A (1983) Crystallization kinetics in the system CaMgSi<sub>2</sub>O<sub>6</sub>–CaAl<sub>2</sub>Si<sub>2</sub>O<sub>6</sub>: the delay in nucleation of diopside and anorthite. *Am Mineral* 68:687–698
- Turner S, George R, Jerram DA, Carpenter N, Hawkesworth C (2003) Case studies of plagioclase growth and residence times in island arc lavas from Tonga and the Lesser Antilles, and a model to reconcile discordant age information. *Earth Planet Sci Lett* 214:279–294
- Uhlmann DR, Klein LC, Handwerker CA (1977) Crystallization kinetics, viscous flow, and thermal history of lunar breccias 67975. In: *Proc Lunar Sci Conf 8<sup>th</sup>*, pp 2067–2078
- Underwood EE (1970) *Quantitative stereology*. Addison-Wesley Pub. Co., Reading
- Vona A, Romano C, Dingwell DB, Giordano D (2011) The rheology of crystal-bearing basaltic magmas from Stromboli and Etna. *Geochim Cosmochim Acta* 75:3214–3236. doi:[10.1016/j.gca.2011.03.031](https://doi.org/10.1016/j.gca.2011.03.031)
- Voorhees PW (1992) Ostwald ripening of two-phase mixtures. *Annu Rev Mater Sci* 22:197–215. doi:[10.1146/annurev.ms.22.080192.001213](https://doi.org/10.1146/annurev.ms.22.080192.001213)
- Walker D, Kirkpatrick RJ, Longhi J, Hays JF (1976) Crystallization history of lunar picritic basalt sample 12002: phase-equilibria and cooling-rate studies. *Geol Soc Am Bull* 87:646–656. doi:[10.1130/0016-7606\(1976\)87<646](https://doi.org/10.1130/0016-7606(1976)87<646)
- Zieg MJ, Lofgren GE (2006) An experimental investigation of texture evolution during continuous cooling. *J Volcanol Geoth Res* 154:74–88. doi:[10.1016/j.jvolgeores.2005.09.020](https://doi.org/10.1016/j.jvolgeores.2005.09.020)
- Zieg MJ, Marsh BD (2002) Crystal size distributions and scaling laws in the quantification of igneous textures. *J Petrol* 43:85–101